FINAL

IN-35 ...

JJ-T

030602

Final Report

A Dual-Line Detection Rayleigh Scattering Diagnostic Technique for the Combustion of Hydrocarbon Fuels
(NAG3-1301)

and

Filtered UV Rayleigh Scattering for Gas Velocity Measurements
(NAG3-1690)

Prepared by
Prof. M. Volkan Otugen
Mechanical, Aerospace & Manufacturing Engineering
Polytechnic University
Six Metrotech Center
Brooklyn, NY 11201

Table of Contents:

I. Abstract

Non-intrusive techniques for the dynamic measurement of gas flow properties such as density, temperature and velocity, are needed in the research leading to the development of new generation high-speed aircraft. Accurate velocity, temperature and density data obtained in ground testing and in-flight measurements can help understand the flow physics leading to transition and turbulence in supersonic, high-altitude flight. Such non-intrusive measurement techniques can also be used to study combustion processes of hydrocarbon fuels in aircraft engines. Reliable, time and space resolved temperature measurements in various combustor configurations can lead to a better understanding of high temperature chemical reaction dynamics thus leading to improved modeling and better prediction of such flows. In view of this, a research program was initiated at Polytechnic University's Aerodynamics Laboratory with support from NASA Lewis Research Center through grants NAG3-1301 and NAG3-1690. The overall objective of this program has been to develop laser-based, non-contact, space- and time-resolved temperature and velocity measurement techniques. In the initial phase of the program a Nd:YAG laser-based dual-line Rayleigh scattering technique was developed and tested for the accurate measurement of gas temperature in the presence of background laser glare. Effort was next directed towards the development of a filtered, spectrally-resolved Rayleigh/Mie scattering technique with the objective of developing an interferometric method for time-frozen velocity measurements in high-speed flows utilizing the uv line of an Nd:YAG laser and an appropriate molecular absorption filter. This effort included both a search for an appropriate filter material for the 266 nm laser line and the development and testing of several image processing techniques for the fast processing of Fabry-Perot images for velocity and temperature information. Finally, work was also carried out for the development of a new laser-based strain-rate and vorticity technique for the time-resolved measurement of vorticity and strain-rates in turbulent flows.

1

II. Introduction:

Reliable and accurate non-intrusive measurement techniques are important in the development of new generation military and commercial aircraft with improved performance envelope. In the military arena, the future aircraft are expected to have superior maneuverability, faster speed and longer range, compared to the current generation of aircraft. The commercial transport of the near future is expected to fly at higher altitudes with supersonic speeds. Furthermore, the emission levels from these aircraft must be reduced significantly in order to avoid a negative impact on the upper atmosphere. Significant research and development efforts are needed in order to realize these goals.

A better understanding of flow physics of transition and turbulence in compressible flows together with the management of turbulence in high-speed aerodynamics will play an important role in achieving the goals described above. Accurate, time-resolved measurement of gas velocity, temperature and density is needed for a better understanding of flow physics. Also, these type of high-quality measurements can provide the data base needed for validation of computer codes developed as design tools. The measurement efforts will have to include ground testing as well as in-flight measurements where laser-based measurements will have to play an important role. New approaches as well as improvements to existing methods are needed to obtain quantitative time-resolved flow data with sufficient accuracy for a diverse set of test conditions

In view of the above, a research program was initiated at Polytechnic University which aimed to develop laser-based diagnostics for gas flows. The program took advantage of the extensive high-speed wind tunnel facilities in the Aerodynamic Laboratory located on the Long Island campus of the University. The overall objective of this program has been to develop laser-based, non-contact, space- and time-resolved temperature and velocity measurement techniques.

During the initial phase of the program a Nd:YAG laser-based dual-line Rayleigh scattering technique was developed and tested for the accurate measurement of gas temperature in the presence of background laser glare. The method improves the applicability of Rayleigh scattering as a temperature/density (or pressure) probe under realistic test conditions such as in combustors where laser glare scattered form walls and windows can be a serious challenge, particularly since the measured quantity depends on the intensity of the Rayleigh scattered light. The technique can be used for both low-speed and high-speed flow conditions, but it is most suitable for low-speed flows since it is more difficult to suppress laser glare at low speeds where the Doppler shift in the signal due to flow velocity is relatively small. An optical system was designed, built and extensive measurements were carried out to determine the effectiveness of the dual-line technique. These experiments showed that considerable improvements are realized in measurement accuracy when both 532 nm second and 266 nm fourth harmonic lines of the Nd:YAG laser are used simultaneously to collect the Rayleigh scattered light. These improvements came in both pressure measurements in vacuum cells and temperature measurements in a heated air jet.

In the second phase of the research program, effort was directed towards the development of a Rayleigh scattering velocity probe for high-speed velocity diagnostics which is based on the shorter wavelengths of a narrow line Nd:YAG laser, including the

2

266 nm uv (fourth harmonic) line. The work focused on identifying possible molecular filter material that has sharp absorption lines near the uv lines of the laser and thus could be used to block out the unshifted laser glare (similar to iodine vapor used in conjunction with the 532 nm green line of the Nd:YAG laser). This development activity concentrated around benzene and its derivatives as possible candidates. The several materials (in vapor form) studied at various temperatures and vapor pressures yielded little encouraging results primarily because the bands initially identified as potentially useful did not yield fine absorption structure in the tunable range of the laser. Nor have the tests revealed any "heads" of a spectral band in this tuning range.

Research was also carried out in the area of interferometric Rayleigh and Mie scattering for the velocity diagnostics of high-speed flows using Fabry-Perot inteferometry. This effort focused on the development of image processing methodologies in order to determine, on-line, the Doppler shift in Mie or Rayleigh scattered light from the measurement volume. In order to achieve this, the scattered light from the probe volume is mixed with unshifted reference laser light before passing it through the Fabry-Perot interferometer. The concentric double-ring pattern obtained at the output of the interferometer is imaged on the CCD camera and subsequently analyzed. Several analysis methods are developed and tested for speed and accuracy in determining the velocity of the high-speed gas.

Lastly, a new concept for a laser-based strain-rate and vorticity measurements was developed and preliminary studies were carried out that confirmed the viability of this novel technique. The technique is based on the collection and heterodyning of scattered light from two closely spaced spots in a transparent fluid. This allows the determination of a component of the strain-rate tensor. Small seed particles are used as scatterers and a single laser is used to interrogate the two spots that form the probe. The heterodyning is achieved directly on a photomultiplier tube and the beat frequency is determined using a standard LDA processor. Several experiments were carried out both using a rotating wheel with a known rpm and a laminar axisymmetric flow between two concentric cylinders with results closely matching those from theoretical (exact) solutions.

III. Dual-Line Detection Rayleigh Scattering Studies

Rayleigh scattering is an attractive technique for the non-intrusive measurement of gas flow properties such as density, temperature, mixture concentration and, in the case of high-speed flows, velocity. Compared to other molecular scattering methods, it is relatively easy to set up and the interpretation of the data is straightforward. It can provide space- and time-resolved information about the flowfield. The technique has been used in both reacting and non-reacting flows, in most cases with considerable success. For example, Rayleigh scattering was used to measure density and temperature in external, premixed jet flames[1-4]. In non-reacting flows, it has been used to measure concentration in binary gas jets[5-8] and temperature in heated jets[9]. In all these experiments, the intensity of the Rayleigh scattered light is measured to determine both the density (or concentration) and the temperature of the interrogated gas. More recently, Rayleigh scattering has been applied to high-speed flows as a velocity probe[10-13]. In this application, a narrow-line laser is used and the central Doppler shift of the Rayleigh scattered light is related to the gas velocity. The spectral characteristics of the Rayleigh signal can also be used to determine gas temperature and pressure[14].

When Rayleigh scattering has been applied to external flows, results have generally been more successful than when the method has been attempted in enclosed environments. In external flows, it is relatively easy to control the surface scattered laser light (or glare) which can potentially contaminate the Rayleigh scattering. In internal flows, surface-scattered laser light is stronger due to multiple reflections from test section walls and optical windows and can therefore generate background levels high enough to contaminate the Rayleigh signal. In particular, if the Rayleigh scattered light is collected at near-forward or near-backward angles, this background noise can completely overwhelm the signal. When the flow velocity is high enough to generate a significant Doppler shift in the Rayleigh scattering spectra, the unshifted background noise can be eliminated by using sharp-edged gas molecule absorption filters. For example, iodine molecular filters have been used in conjunction with Nd:YAG lasers for Rayleigh scattering measurements in supersonic wind tunnels[12,14]. However, in most low-speed flows, such as those in combustors, the Rayleigh scattered light from the gas molecules and surface scattered background noise have approximately the same central frequency and, therefore, such filtering techniques cannot be used.

Ötügen et al.[15] presented a dual-line detection Rayleigh scattering (DLDR) technique to address the problem of signal contamination by surface-scattered laser light. They used the two lines of a copper-vapor laser with a single set of transmitting and collecting optics to capture and analyze signal from both the 578 nm yellow and 510 nm green lines. In this technique, a two equation system is formed with the Rayleigh scattering signal and background noise as the two independent variables, thus enabling the determination of background noise due to laser glare, which can be removed from the Rayleigh signal. Using this copper-vapor laser-based system, they obtained relatively accurate temperature measurements even when the background level bas twice that of the Rayleigh scattered signal. The present research aims to improve this technique by extending it to Nd:YAG lasers.

The basic motivation of the work is that copper-vapor lasers are limited in their applicability to Rayleigh scattering in that they offer relatively low pulse energies

compared to Nd:YAG lasers. The high pulse energies of Nd:YAG lasers are better suited for time-resolved measurements and also provide better beam characteristics. In this present effort, a Nd:YAG laser-based DLDR system is developed and tested under a diverse set of conditions. The system uses the 532 nm second and 266 nm fourth harmonics of the laser and a single set of transmitting and collecting optics is used to form the probe and to collect scattered light from it. The system was calibrated and tested under several background noise levels using both a vacuum chamber and a heated air jet as the test environment. Finally, turbulent temperature measurements were made in a hot air jet and results were compared to those obtained by a fast-response thermistor in the same jet. An analysis was also carried out to estimate the uncertainty characteristics of the system. The single-shot measurement uncertainty determined from shot-noise statistics compared favorably with the statistics of the actual measurements.

3.1. Overview of the Dual-Line Detection Technique:

A single beam containing two lines of the laser is used in the DLDR technique. The Rayleigh scattered light from the probe volume is collected and collimated using a single lens. Subsequently, the signals from the two lines are separated using a dichroic splitter and sent to separate detectors providing a linear system of two equations with Rayleigh scattered light energy and background noise as two unknowns; both normalized with the laser energy at the appropriate line. The two equations are independent and lead to a unique solution since the wavelength dependence of Rayleigh scattered light and surface scattered light are different. Still, the greater the disparity between the two wavelengths, the more robust the system. Therefore, the present system using the second and fourth harmonic lines of the Nd:YAG laser is superior to the earlier copper-vapor laser-based system which used the 578 nm and 510 nm lines[15].

Using the equation of state for a perfect gas, the system of equations for the DLDR system can be expressed as follows:

$$\frac{E_{T,1}}{E_{L,1}} = C_1\left(\frac{\sigma_1 P}{\kappa T} + \beta C'\right) \tag{1}$$

$$\frac{E_{T,2}}{E_{L,2}} = C_2\left(\frac{\sigma_2 P}{\kappa T} + C'\right) \tag{2}$$

Here, E_T, the total captured energy is normalized by the incident laser energy, E_L. P and T refer to the gas pressure and temperature while κ and σ are the Boltzmann constant and the Rayleigh scattering differential cross section, respectively. In the present system, 532 nm and λ_2 =266 nm. The system can be calibrated to determine C_1 and C_2, under known pressure and temperature conditions. C' represents the background level and β is the ratio of surface scattering at the two wavelengths which is also determined through the calibration process. Through Eqs. (1) and (2) the system provides a direct measurement of pressure or temperature independent of the background noise. For example, if gas pressure is the quantity to be measured, the above system yields.

5

$$P = \frac{\dfrac{E_{r,1}}{E_{L,1}}\dfrac{1}{C_1} - \dfrac{E_{r,2}}{E_{L,2}}\dfrac{\beta}{C_2}}{\dfrac{\sigma_1 - \beta\sigma_2}{\kappa T}} \qquad\qquad (3)$$

with

$$C' = \frac{\dfrac{E_{T,2}}{E_{L,2}}\dfrac{\sigma_1}{C_2} - \dfrac{E_{T,1}}{E_{L,1}}\dfrac{\sigma_2}{C_1}}{\sigma_1 - \beta\sigma_2} \qquad\qquad (4)$$

Equation (4) does not provide any information regarding the flow, but it serves the purpose of determining the reliability of a measurement. Although Eqs. (3) and (4) completely decouple pressure and background, there is a threshold value of C' for each system above which, reliable measurements are not possible mainly due to the saturation of one or more of the electronic/optical components of the system. Once this threshold value of C' is determined through the initial calibration, it can be used as a flag against unreliable measurements.

3.2. The Optical System:

The optical arrangement for the DLDR system is shown in Fig. 1. The output of the laser at the 1064 nm fundamental frequency is doubled through a harmonic generator to produce the 532 nm second harmonic. The residual infrared is removed from the 532 nm green line using a harmonic separator and directed into a beam dump. The green line is passed through a fourth harmonic generator where the frequency is again doubled to generate 266 nm UV line along with the residual 532 nm light. The green and the UV lines are polarized at 90 deg. to each other. The half-wave plate before the fourth harmonic generator is rotated such that the polarization direction of the second and fourth harmonic lines are ±45 deg. to the direction along which the Rayleigh scattered light is collected. Since Rayleigh scattering cross-section has a sine function dependence on this angle, the arrangement provides optimum Rayleigh scattering signal when using both lines simultaneously. A quartz achromatic lens focuses the beam to form the probe volume. This lens is specifically designed for the second and fourth harmonics of the Nd:YAG laser and has the same focal length (400 mm) for both the green and the UV lines hence making the beam waist (probe volume) of the two lines coincident. The laser is operated at 10 Hz repetition rate and under this condition, the conversion efficiency of the fourth harmonic generator is only about 14 percent. The pulse energies at the probe are measured to be 8.8 mJ and 1.2 mJ for the 532 nm and 266 nm lines, respectively. However, since the Rayleigh scattering cross-section for the UV line is 16 times that for the green, the Rayleigh signal from the UV line is still twice as strong. The laser beam is terminated inside a beam dump past the probe volume.

6

The Rayleigh scattered light from the probe volume is collected by a 300 mm focal length quartz lens and at a 90 deg. angle to the propagation direction of the beam. The collimated light is color-separated using a dichroic splitter and, the signal from each line is sent to a separate photomultiplier tube (PMT). Before entering the pinhole and the PMT, each signal is passed through an interference filter at the appropriate wavelength to prevent signal cross-talk and to discriminate against broadband background. To account for the pulse-to-pulse energy variation of the laser, the Rayleigh signal is normalized by the laser output at each shot of the laser. To accomplish this, a small portion of the laser beam is split just before the achromat that forms the probe volume (Fig.1) and subsequently color separated using a second dichroic splitter. The laser light from each line is fed to a photodiode, the output of which is sampled along with those of the PMTs during each shot of the laser.

The PMT output of Rayleigh scattering signal and the laser reference output from the photodiodes are fed to sample-and-hold units and subsequently digitized by a 12-bit, 8-channel analog-to-digital converter. The digitized data is stored in a personal computer for post processing. Video amplifiers are used to optimize the individual outputs from the PMTs. Data is collected from all four channels at each pulse of the laser (10 Hz repetition rate), which is processed to yield local, time-frozen temperature or pressure. A trigger pulse, synchronized with the Q-switching of the laser, initiates the data sampling. A schematic of the signal processing scheme is shown in Fig. 2.

3.3. System Calibration:

The Rayleigh scattering system was calibrated several times under different sets of conditions. The temperature calibrations were undertaken using a hot air jet. The system was also calibrated against gas pressure using a vacuum chamber. In each case, the calibration procedure was repeated several times with various levels of laser line background in the collected signal in order to determine the value of the surface scattering ratio, β, and to assess the effect of background level on calibration accuracy.

Figure 3 shows the general arrangement for the jet calibrations. The hot air jet has an inner core whose temperature can be controlled and a surrounding co-flow that is kept at ambient temperature. The supply air to the jet is filtered in order to eliminate patriculates in the flow, thus avoiding the contamination of the Rayleigh signal by Mie scattering. The laser probe is positioned at the centerline of the jet, approximately two inner jet diameters downstream from the exit plane. The jet temperature is measured by a thermistor which is placed immediately downstream of the laser probe.

Figure 4 shows two representative calibration curves obtained using the jet whose temperature was varied between 290 K and 780 K. Different levels of background noise were obtained by scattering some of the laser light from an aluminum plate placed within the line of sight of the collecting optics, on the opposite side of the probe volume. Each data point in the figure is an average of 1000 shots of the laser. The normalized Rayleigh signal grows linearly with inverse temperature while background due to laser glare adds a bias to the collected signal. Obviously, if not accounted for, this bias can cause large errors in temperature measurements. For both sets of calibrations, the scatter in the data is quite small; the relative standard deviation for Fig. 4(a) is 3.6 while this value is 4.6 in Fig. 4(b). The effect of background contamination on the green line is more pronounced due to the

7

smaller Rayleigh scattering cross-section at this wavelength. The scattering cross-section increases with shorter wavelengths resulting in higher signal energies in the UV, and thus, lower levels of relative background compared to the green line. The results of the air jet calibrations are summarized in Table 1. These results represent six individual calibrations similar to the two shown in Fig 4, each with a different background level.

The vacuum chamber used for the pressure calibrations is of the cross-hair type, consisting of two hollow orthogonal cylinders which intersect at the center of the chamber. Quartz windows are placed at the ends of each cylinder. The laser beam travels through one cylinder forming the probe volume at the crossing of the two cylinders. The scattered light is collected through one window of the other cylinder. An aluminum plate is placed outside of the opposite window which is used to scatter laser glare into the test chamber. When the plate is removed from the window, the Rayleigh signal is free of background noise. Figure 35 shows two representative calibrations; (a), with no background noise present in the Rayleigh signal and (b), Rayleigh signal with some background contamination. Each data point on the graph represents an average of 1000 individual realizations. These pressure calibrations also show a linear dependence of signal on gas pressure with little scatter in the data. Again, the UV signal is much less sensitive to the background noise than the green line is. The results of six sets of pressure calibrations with varying levels of background noise are summarized in Table 2. The calibration constants in Table 2 are very close to those obtained earlier through temperature calibrations and summarized in Table 1, indicating that both procedures can be used to obtain accurate calibrations. In both cases, the uncertainty due to random scatter in data is small giving further confidence in the optical system and the calibration procedures. Another important outcome of the calibrations is the value of β, which is approximately 2 in both calibrations. This indicates that surface scattering of the laser light in the UV line is only half as strong as in the 532 nm green line. Therefore, since the Rayleigh scattering cross-section has λ^{-4} dependence on the wavelength, the signal-to-background noise ratio of the UV line is about 32 times larger than the green line.

Using the results in Tables 1 and 2, an analysis is carried out to assess the reliability of the optical system in the measurement of vacuum pressures. In single-shot measurements, the two primary sources of error are shot noise and the uncertainty in the calibration constants. For single-line detection, the relative error in pressure due to the uncertainty in C is given by

$$\frac{\Delta P}{P} = \frac{\left(\dfrac{E_T}{E_L}\right)\left(\dfrac{1}{C^2}\right)}{\left(\dfrac{E_T}{E_L}\right)\left(\dfrac{1}{C}\right) - C'} \tag{5}$$

while for the dual-line operation, this error can be expressed as

8

$$\frac{\Delta P}{P} = \frac{\left[\left(\frac{E_{T,1}}{E_{L,1}}\frac{1}{C_1^2}\right)^2 (\Delta C_1)^2 + \left(\frac{E_{T,2}}{E_{L,2}}\frac{\beta}{C_2^2}\right)^2 (\Delta C_2)^2\right]^{\frac{1}{2}}}{\frac{E_{T,1}}{E_{L,1}}\frac{1}{C_1} + \frac{E_{T,2}}{E_{L,2}}\frac{\beta}{C_2}} \tag{6}$$

In the above equations, ΔP and ΔC represent the uncertainty in pressure and coefficient C, respectively. Since the background noise is determined explicitly and eliminated from the Rayleigh signal in DLDR technique, C' has no influence on the relative error in pressure and hence, does not appear in Eq. (6). For the present system, the relative error in pressure becomes $\Delta P/P \approx 0.035$, in the absence of background noise. The error in pressure due to calibration uncertainty is shown in Fig. 6 along with that due to photon shot noise (for single-shot measurements). The background level is assumed to be zero for the single-line detection. The shot noise error is due to the uncertainty in the number of detected photons at each measurement and is calculated from Poisson statistics[15]. For single-line Rayleigh scattering measurements

$$\frac{\Delta P}{P} = \frac{\left(\frac{hc}{\lambda}E_T\right)^{\frac{1}{2}}}{\left(\frac{E_T}{E_L}\frac{1}{C} - C'\right)CE_L} \tag{7}$$

For the DLDR method, the relative error in pressure due to shot noise is given by

$$\frac{\Delta P}{P} = \frac{\left[\left(\frac{kT}{E_{L,1}C_1(\sigma_1 - \beta\sigma_2)}\right)^2\left(\frac{hc}{\lambda_1}E_{T,1}\right) + \left(\frac{\beta kT}{E_{L,2}C_2(\sigma_1 - \beta\sigma_2)}\right)^2\left(\frac{hc}{\lambda_2}E_{T,2}\right)\right]^{\frac{1}{2}}}{\dfrac{\frac{E_{T,1}}{E_{L,1}}\frac{1}{C_1} - \frac{E_{T,2}}{E_{L,2}}\frac{\beta}{C_2}}{\frac{\sigma_1 - \beta\sigma_2}{kT}}} \tag{8}$$

Here, h is Planck's constant and c is the velocity of light.

For the present optical system, the contribution of the calibration constant uncertainty to the overall measurement error is relatively small (≈ 3.5 percent) for both single-line and dual-line operation. On the other hand, the shot noise error has a strong dependence on gas pressure at low pressures. This is due to the fact that the Rayleigh scattered energy decreases with decreasing gas pressures which in turn increases the relative shot noise. It is also noted that measurement error due to shot noise is larger for the dual-line detection method as compared to the single line operation. The laser used for the present study has a relatively low pulse energy (approximately 10 mJ) compared to the

9

new generation Nd:YAG lasers which can produce pulse energies of the order of a Joule. Even then, the shot noise uncertainty level of the present DLDR system is significantly lower than that of the previous copper-vapor laser-based system[15]. For example, at 760 torr, the relative uncertainty of the present DLDR system is calculated to be 2 percent while, this number for the copper-vapor based system is about 5 percent. At a vacuum pressure of 20 torr, these levels become 13 percent and 35 percent for the Nd:YAG- and copper vapor -based systems, respectively. Clearly, at this pressure, it is not possible to obtain reliable single-shot measurements using the latter system.

3.4. Pressure Measurements:

Figure 7 compares pressures measured by the DLDR system to those obtained using a gage in the vacuum chamber. Pressure measurements were obtained at each shot of the laser and each data point in the figure correspond to the average of 1000 such pressure realizations. The agreement between the two sets of measurements is strong although most of the Rayleigh data fall slightly below the straight line which represents a perfect agreement between these measurements and those from the vacuum gage indicating that the DLDR measurements slightly underestimate the pressure. The rms of the 1000 individual pressure realizations are shown in the figure as solid-line error bars. These measured uncertainties are slightly larger than those estimated using Eq. 8, which are shown as dashed bars in the same figure. Electronic noise also contributes to the measurements uncertainty in addition to the shot noise, thus leading to slightly larger uncertainties than those estimated.

Pressures obtained using the DLDR method are compared to those from single-line detection Rayleigh scattering in Fig. 8. The Rayleigh scattered signal is intentionally contaminated by surface-scattered background noise. The results closest to those of the vacuum gage are obtained by the DLDR method. The UV single-line detection results are also close to those of the vacuum gage, although they are slightly but consistently larger due to the background contamination. The single-line detection using the 532 nm green line gives, by far, the poorest results. The background noise nearly overwhelms the Rayleigh signal in the green line although its effect on the UV signal is still small. Therefore, for single-line operation, the UV line should be the choice for better signal-to-background noise characteristics although if measurements with the highest possible level of accuracy are needed, the dual-line detection technique is preferable.

Figure 9 shows pressure results obtained by the DLDR system under different levels of background. These measurements were made in order to determine the maximum level of background noise-to-Rayleigh signal ratio under which reliable gas pressures can be obtained. These measurements were made at a fixed cell pressure of 505 torr (measured by the vacuum gage) and under several background levels. The air temperature in the chamber was kept at 298 K. Under these conditions, the average Rayleigh scattered signal is constant while the background contamination level is varied. In Fig. 9, the signal-to-noise levels are based on the 532 nm green line. The Rayleigh scattered energy, $E_{R,l}$, is calculated using gas pressure measured by the vacuum gage while the background is determined from the DLDR measurements (Eq. 4). Again, each data point represents an average of 1000 pressure realizations obtained at each shot of the laser. The figure indicates that accurate pressure measurements are possible even when the

background noise-to-Rayleigh signal ratio is as high as three. For ratios $E_{B,1}/E_{R,1} > 3$, the system over-estimates the gas pressure, most likely due to the saturation of the photomultiplier tube for the green line at this light level. The corresponding background-to-signal ratio in the 266 nm line is still significantly smaller $(E_{B,2}/E_{R,2} \approx 0.1)$ since the signal-to-noise characteristics of the UV line 32 times better that of the green, as pointed out earlier. Therefore, under the same background conditions, if only the UV line were to be used for detection, instead of the dual line method, the pressure would be overestimated by approximately ten percent.

3.5. *Temperature Measurements:*

The temperature measurements were made in the heated air jet described earlier. Instantaneous temperatures were obtained at each shot of the laser in the initial development region of the heated jet in the presence of different levels of background laser glare. From long records of these instantaneous temperatures, radial and axial distributions of mean and turbulent temperature were obtained. These results are compared to those obtained using single-line Rayleigh scattering measurements as well as to those from a fast-response thermistor. Figure 10 shows the mean temperature distribution across the co-flowing jet seven diameters downstream of the exit. In the Rayleigh scattering measurements, the signal is intentionally contaminated by laser glare to test the optical results. The same method as in the jet calibrations is used for background contamination. The record length for each data point is 3000 in both the Rayleigh scattering and the thermistor results. Figure 10 indicates that the thermal jet goes through a rapid initial development; the temperature profile at x/d = 7 has a nearly-Gaussian profile, which is a characteristic of the self-preserving jet. The DLDR results agree very well with those of the thermistor while both the UV and the green line-only results underestimate the jet temperatures due to the background noise. However, while the 532 nm single-line errors are unacceptably large for any practical application, the errors in the 266 nm single-line detection are relatively small.

The turbulent temperature profile obtained by the DLDR system at x/d = 7 is shown in Fig. 11 along with the corresponding thermistor result. The two measurements are in good agreement although, on the average, the DLDR measurements give slightly higher results than those of the thermistor. This is partially due to the effect of shot noise which tends to increase rms of temperature. The turbulent temperature profile agrees well, both quantitatively and qualitatively, with previous results of heated air jets with the maximum intensities located around maximum mean temperature gradients.

The axial distribution of the inverse of jet centeraline mean temperature is shown in Fig. 12. The jet temperature on jet centerline,T_j is referenced to the initial co-flow temperature and normalized by the jet exit excess temperature. The agreement between the thermistor and DLDR results are remarkably good. On the other hand, the green-only Rayleigh scattering results completely fail in predicting the mean centerline temperature distribution, overestimating the decay rate essentially starting from the jet exit. The UV-only results follow those of DLDR and the thermistor fairly well, only slightly overpredicting the decay rate of centerline temperature. All three sets of results show a linear growth for the inverse temperature with axial distance with a slope of approximately 0.165, based on the DLDR and thermistor results. This slope is slightly larger (0.18) for

11

the UV-only results. The corresponding rms temperature distributions are shown in Fig. 13. Here, only the thermistor and DLDR results are compared. The agreement between the two sets of data is again good. As mentioned earlier, while the DLDR data is slightly higher in the initial jet region the reverse is true for $x/d>15$. The growth rate of the temperature fluctuations at the jet centerline is slow when compared to other studies of fluctuating passive scalars in turbulent round jets. This may be attributed to the difference in the initial velocity distributions. In the present, the jet exit velocity profile is fully developed, while in most jets for which turbulent transport of scalars are reported, the initial velocity has a top hat profile with a small boundary layer at the nozzle wall which leads to a faster initial growth rate of turbulence. Another complicating factor is the coflow which has the effect of retarding the overall growth of the jet.

IV. Material Testing for UV Rayleigh Scattering

4.1. Objective:

The primary goal of this effort is to develop a Rayleigh velocity probe for high speed velocity diagnostics which is based on the shorter (uv) wavelengths of a injection seeded narrow-line Nd:YAG laser and with superior background rejection capability. The focus here is to identify a molecular absorption filter (low pressure, gas phase) to be used in conjunction with the 266 nm fourth harmonic of the laser. The optical setup is similar to the iodine vapor filter which has recently become quite popular in Rayleigh and Mie scattering measurements using the 532 nm second harmonic of the Nd:YAG laser or the green line of an Argon-ion laser. Therefore, a good candidate for filter must have a fine absorption structure in the vicinity of 266 nm. Such material could have a significant impact on the capability of Rayleigh scattering as a high-speed velocity and possibly temperature probe. In many practical applications, laser light scattered from various surfaces and windows, for example, in wind tunnel experiments. When the flow velocity is high enough to generate a Doppler shift relative to the laser's central frequency, this unshifted noise can be removed from signal using an absorption filter. For Rayleigh scattering, using shorter laser wavelengths provide a significant advantage since the Rayleigh scattering cross-section has an inverse fourth power dependence on the laser wavelength making the signal intensities much stronger in the uv. Furthermore, scattering/reflections from solid surfaces diminish with shorter wavelengths as discussed in the previous section (Section III). Therefore, the gain in signal-to-background noise ratio is quite significant (in the vicinity of 32 folds improvement from 532 nm to 266 nm) when the 266 nm line of the Nd:YAG laser is used instead of the 532 nm green line. Again, a more detailed discussion of this point accompanied with some results can be found in Section III. However, there is still need for a suitable filter material for the 266 nm line particularly for use in wind tunnel experiments under non-ideal conditions with such as scratched windows, etc.

4.2. Test Setup:

An injection seeded Nd:YAG laser was used for the experiments. The seeding is provided by a diode laser at 1064 nm which is also the fundamental frequency of the host YAG laser. The frequency of the diode laser and hence that of the host laser can be tuned in a narrow range by hanging the crystal temperature of the diode. Therefore, it provides a means to interrogate the absorption characteristics of the tested material. The laser is frequency doubled and subsequently quadrupled to obtain, simultaneously, the 532 nm green and 266 nm uv lines which are both used for the experiments. Note that there is no cross-contamination of different harmonics.

Figure 14 shows the general setup of the optics. After the second harmonic generating crystal, the 1064 nm infrared is completely removed from the green line. Then the green is again frequency doubled and the green and uv lines are separated into two beams. The green line is used as a reference (in order to determine the exact frequency of the laser at any given time) in conjunction with a Fabry-Perot interferometer. While the 266 nm uv line interrogates the filter material (in gas phase at low pressures) contained in an optical cell. As shown in Fig. 14, the uv beam is split in two. One beam goes through

the absorption cell filled with the test material before it hits the pmt while the other is shone directly on another pmt. The output of the second pmt is used as a reference and the relative energy through the cell is determined by normalizing the output of the first pmt by that of the reference. This is done in order to avoid the effects of pulse-to-pulse energy fluctuations of the laser in uv as well as that from the longer term drift in laser output. The output of each pmt is fed into two separate channels of a boxcar averager before being processed. In any case, the absorption measurements are made by looking at averages of several shots of the laser. The interference pattern of the Fabry-Perot instrument (in green) is imaged on a CCD camera. This provides the frequency change information as the diode laser is slowly tuned across its total range. The optical cell is made of an aluminum cylinder with a quarts window at each end.

A typical tuning of the laser viewed by the Fabry-Perot interferometer is shown in Fig. 15 while the a corresponding diode crystal temperature versus frequency shift calibration curve is given in Fig. 16. These measurements were made in the green 532 nm line as also indicated in Fig.14. The Fabry-Perot interferometer is operated in the Freseau mode where the output plate is slightly misaligned relative to the front mirror so that nearly linear fringes are obtained as opposed to the familiar "bullseye" circular pattern. Several fringes are tracked as the seed laser crystal temperature is varied by changing its input voltage. The ordinate in Fig. 15 shows the pixel location of the fringes as they are displaced with changing laser frequency. At any given frequency, at least three fringes are present in the image and the maximum number of fringes per image is four as seen in the figure. In order to determine the frequency shift at each crystal temperature, the average displacement of the fringes is obtained in each image. The frequency is obtained by comparing the displacement to the free spectral range (the distance between two consecutive fringes) of the interferometer. Figure 16 clearly shows that the tunable range of the laser is approximately 35 GHz. Outside of this range, the host laser output does not lock into a single, stable frequency and runs with multiples of longitudinal modes. The figure also shows that, for the most part, the laser frequency is a linear function of the crystal input voltage. There is a small jump around 2.8 Volts but on either side of this jump, the graph is quite linear and repeatable.

Figures 17 and 18 show the stable and unstable modes of the laser at two adjacent crystal input voltages. These are a single row output of the Fabry-Perot images. In Fig. 16, the input voltage is approximately 3.25 Volts and the laser output is stable as three distinct fringes are captured. When this voltage is slightly increased, a secondary frequency appears as seen in Fig. 17 and the laser output is unstable. Therefore, care must be taken in operating at the edges of the stable range of the laser.

Figure 16 shows only the tunability range and not the exact frequency of the laser. The exact frequency (or wave number) is obtained by passing the same laser beam (green) through an iodine cell under a known set of pressure and temperature conditions. Then, the absorption pattern through the iodine cell is compared to the Forkey[16] (Princeton University) computer model in order determine the exact frequency range of the laser.

4.3. *Materials tested and Results:*

The testing activity concentrated around the benzene and its derivatives. Benzene and its derivatives are the group of organic molecules that have strong absorption bands in

the general region which overlaps the tunability range of the fourth harmonic line of the Nd:YAG laser. The first absorption band of benzene is centered around 255 nm. It is followed by more than 30 bands shifted towards shorter wavelengths. The gas absorption spectrum of benzene looks similar to that of iodine in the visible range with some fine structures. The substitution on the benzene ring by auxochromatic groups or by hyboges reduces the symmetry of the new molecule. This change results in the red-shift of the spectral bands as well as an increase in the absorption intensity. Therefore, most benzene substitutes are potentially strong absorbers around 266.1 nm. On the downside, as the test results indicate, some of the spectral bands can sometimes result in the reduction of the fine structures which are essential for the present application.

In order to applicable for Rayleigh scattering, the absorption lines of the molecular filter has to have sharp (or fine) spectral structures in the laser's tunable range. His can be a single isolated spectral line or a sharp "head" of an absorption band. The ultraviolet absorption spectra of gas phase benzene derivatives are available in the literature. However, the resolution (spectral) of the data is far too poor to be useful for Rayleigh scattering applications.

Unfortunately, these tests did not show any promising structures in the frequency range of our laser. Tests were repeated at several gas pressures and temperature ranges for each of the selected chemicals. In most cases, either a broad partial absorption (between 10% and 65% absorption) was observed across the tuning range or the absorption was near 100% with no fine structures. Unfortunately, even at the lowest pressures and temperatures (1 torr and 273 K, respectively) no fine structures were detected.

Table 3 gives all the chemicals that were considered as candidates for rejection filter while Table 4 shows only those that were actually tested. The tests for each chemical was repeated several times at different temperatures and pressures. The vapor pressure was varied in the range 50 torr and 1 torr while the gas temperature was varied in the range between 325 K and 273 K. Before each experiment the cell was purged by air and then evacuated by a vacuum pump. Then, into a side arm, through a septa and syringe injector, the liquid chemical was introduced. Then the valve connecting the side arm to the main cell was opened and the vapor of the chemical was introduced. The temperature of the side arm was the primary controller of the amount of vapor let in the cell and hence the pressure. A heating/cooling pad along with a bath system was used to control the cell temperature. Several strategically placed thermocouples monitored and controlled the cell temperature. The pressure and temperature range in the study was purposefully chosen as to be realistically and easily applicable in practice. A very elaborate cell system may not be suitable for practical applications. Thus, this limited the range of possibilities (pressure and temperature) for the different chemicals. As an example, the vapor temperature-pressure graph of the fluoro-toluene family and several halogens are shown in Figs. 19 and 20, respectively. It is clearly seen that in several cases, for practically obtainable vacuum pressures, the minimum temperature for vapor can be quite high.

During these studies, several problems were encountered. Firstly, the large laser energies altered the optical characteristics of the gas phase chemicals. This was observed in the form of non-repeatable results. The problem was overcome by reducing the intensity of the interrogation laser beam through the cell. This eventually resulted in stable

15

chemicals and repeatable results. Another problem was the storage stability of the chemicals. Some of the chemicals (once came into contact with air) showed different absorption levels over a long time period (a week or longer).

Figures 21 through 25 show some of the results of these studies that give a general idea of the absorption patters observed. In all these graphs, the measured intensity is relative. First of all, as pointed out earlier, the output of the pmt which collects light through the cell is normalized immediately by a reference light from the laser to eliminate laser intensity fluctuations. Further normalization is obtained by dividing this value by the value obtained through the cell when it is completely evacuated. This takes into account the absorption by the windows, etc. (Note that in Fig. 20 the jump in the transmission at the high end of the tuning voltage was later determined to be a erroneous and has to be discounted). While fluorotoluen derivatives as well as benzene have a relatively strong absorption characteristics, the derivatives of benzene transmit most of the uv light in this range. What is common to all of these is the fact that there are no structures to the absorption. All other material studied showed basically similar and nearly monotonous absorption characteristics.

V. Image Processing Techniques for Fabry-Perot Interferometry

In this phase of the research, image processing methods have been developed in conjunction with a Fabry-Perot interferometer, in order to determine the local velocity of gas flows. The processing techniques are used for the on-line determination of the Doppler shift in Mie or Rayleigh scattered light form the measurement volume. The scattered light is mixed with unshifted light from the interrogation laser for reference before passing it through the interferometer. The concentric, double-ring pattern image formed at the output of the interferometer is captured by a CCD camera and subsequently analyzed. The original image in polar coordinates is first mapped into a rectangular coordinate system and subsequently analyzed for frequency content using power spectral and cross-correlation methods in order to determine the Doppler frequency. The robustness of the technique has been tested using simulated images under several signal-to-noise conditions.

5.1. Motivation:

Nonintrusive, quantitative diagnostic techniques are needed in high-speed aerodynamics research in order to characterize flow parameters including gas velocity, temperature and density. Techniques are sought both for ground testing and for in-flight measurements. A desirable feature in a technique is the ability to obtain "time-frozen" measurements so that unsteady and turbulent features of the flow can be investigated. Developments are still needed in this area, however, several laser-based techniques have emerged in recent years which show promise for the future.

One of these techniques is the interferometric Rayleigh/Mie scattering in which, the spectral characteristics of the scattered light is analyzed using a Fabry-Perot interferometer[12,14,36,37]. In this technique, a narrow-line laser is used to interrogate a point or a two-dimensional plane in the flow. If Mie scattering is used, the spectral width of the scattered light is essentially the same as that of the incident laser light while, the peak frequency is Doppler-shifted by an amount which is a function of the velocity of the scattering particle as well as the optical configuration. However, the amount of this frequency shift is typically very small for most aerodynamic applications (including supersonic flows) and its accurate determination is difficult. If Rayleigh scattering is used, the line broadening and intensity of the scattered light from the molecules can be related to gas temperature and density providing additional information about the flow field. The Rayleigh scattering-based method has been used in order to assess the viability of this method as a tool for rocket plume diagnostics[12] and for ASTOVL model tests[14]. In both studies, a scanning Fabry-Perot interferometer was used and the data was post processed for time-averaged temperature and velocity. Later, the method was extended by capturing the two-dimensional Fabry-Perot images with a CCD camera. With this approach, instantaneous velocity information was obtained in a supersonic wind tunnel[36] and at the exit of a supersonic jet[37]. In both cases, however, the acquired images were post-processed for velocity after the experiments.

Advanced image processing methods must be employed in order to develop these interferometric techniques into robust, reliable and routine diagnostic tools. First of all, fast, automated analysis of the Fabry-Perot interference patterns is necessary, in order to obtain time-series data. The image captured by the CCD camera can possess poor signal-to-noise characteristics which render the accurate determination of the Doppler shift

17

difficult. Therefore, robust image processing methods are needed in order to maintain levels of measurement resolution that are acceptable for quantitative results. Furthermore, since the Fabry-Perot alignment is highly sensitive to external conditions such as temperature fluctuations and vibration (which tend to exist in both ground and in-flight tests), image analysis techniques that can take into account small degradation in instrument alignment are desirable.

In the present work, several image processing methods have been developed and tested for speed, accuracy and reliability. These methods depend on the linearization of the concentric circular interference rings from a planar Fabry-Perot interferometer and subsequent statistical analysis using both spectral and correlation methods. The optical setup and analysis procedure allows for the determination of the Doppler shift, independent of small drifts in the Fabry-Perot mirror alignment and the incident laser frequency improving the versatility of the technique in practical applications.

5.2. Doppler Shift

Laser light scattered from a moving particle will exhibit a Doppler shift that is dependent on the angle between the incident laser beam and the scattering direction as well as the magnitude of the particle velocity. This principle of light scattering is illustrated in Fig. 26 where k_0 and k_s are the wave vectors for the incident laser light and the scattered light, respectively. The scattered light from a particle with a velocity, V, will be Doppler shifted by an amount $\Delta f = (1/2\pi)(k_s - k_0) \cdot V$. With the assumption that the magnitude of the wave vectors is $2\pi/\lambda$, the Doppler shift can be expressed as $\Delta f = (2V_x/\lambda)\sin(\alpha/2)$ where, λ is the incident laser wavelength and V_x is the component of velocity along the direction $(k_s - k_0)$. Therefore, by judicially placing the laser beam and the collecting optics, one can select a component of velocity to measure. By changing α, one can also control the magnitude Δf and optimize it for a given experiment.

5.3. Fabry-Perot Interferometer

The Fabry-Perot interferometer is essentially made up of two partially transmitting mirrors placed parallel to one another inside a housing. In a plane Fabry-Perot interferometer these mirrors are flat. If the space between the two partially reflecting mirrors is illuminated by a beam of monochromatic light entering through one mirror, the light will be transmitted through the other only when the optical path length between the surfaces is an integral number of the wavelength of the light. Therefore, the interferometer acts as a filter with a transmittance that is dependent on the wavelength of the light, the angle of the incident light beam relative to the surface normal of the mirrors, the refractive index of the medium between the two mirrors, as well as the distance between these mirrors. An in-depth theory of Fabry-Perot interferometers can be found in Vaughan (1989)[38].

The most common way of using the Fabry-Perot interferometer is by moving one mirror relative to the other by piezoelectric means, thereby changing the distance between the two mirrors at a constant speed. In this "scanning" mode of operation, the output is monitored by a light sensor such as a photomultiplier tube and the periodic transmission of light is related to the wavelength. In the scanning mode, time-resolved frequency characteristics of the light cannot be realized. An alternative is to allow the incoming

18

monochromatic light with a certain divergence angle and focus the output light from the interferometer by using a focusing (or "fringe forming") lens. In this case, an interference patter made up of a series of concentric bright rings of the transmitted light is formed at the focal plane of the lens. This image can be captured by a CCD camera[39] and subsequently analyzed for the spectral characteristics of the light. Both the scanning and imaging modes of operation have been used in aerodynamic applications by Seasholtz and co-workers[12,14,36,37].

The free spectral range (FSR) of the interferometer, defined as the frequency range represented by the distance between two consecutive rings, is given by FSR=c/2dn. Here, c is the velocity of light, n is the refractive index of medium between the two mirrors (in the present study, n=1 since room temperature air occupies the cavity of the interferometer), and d is the distance between the two mirrors. Larger FSR and hence, range of measurements can be obtained by reducing the distance between the two mirrors. However, this will also result in reduced measurement resolution. Therefore, the optimum value of d has to be determined taking into account both the velocity range to be measured as well as the optical configuration shown in Fig. 26.

In the present image analysis experiments, a plane Fabry-Perot interferometer is used in conjunction with a focusing lens at the output in order to form the interference pattern of concentric rings. For most measurements, the distance between the mirrors was selected as d = 40 mm which renders a free spectral range of FRS = 3.75 GHz .

5.4. Experimental Setup:

Figure 27 shows the optical arrangement for the present study. A narrow line, pulsed Nd:YAG laser is used as the light source. The fundamental line of the laser is 1064 nm. The 532 nm second harmonic line of the laser, obtained by passing the infrared laser beam through a KDP crystal, is used for the experiments. The line narrowing is obtained by seeding the laser gain in the infrared through a diode laser. The line width at 532 nm green line is estimated to be approximately 120 MHz (half-max, full width). The laser beam passes through Mach 1.65 free jet where the velocity measurements are made. The scattered light from the probe volume is collected at 90 deg. to the laser beam as shown in Fig. 27. Therefore, the Doppler shift in the scattered light is proportional to the streamwise velocity component of the jet.

A small portion of the laser energy at the green line is extracted by a beam splitter before the beam forms the probe volume. This reflected light, which is used for reference frequency during the measurements, is coupled into an optical fiber and is collimated at the exit of the fiber as shown in Fig 27. A second beam splitter combines this reference light with the scattered light from the probe volume before passing them through the Fabry-Perot interferometer. The output of the interferometer is then focused on the CCD camera (using a 540 mm lens) where, the concentric rings of the interference pattern are formed. The reference and measurement beams are aligned such that when there is no flow, interference rings of the signal from the measurement volume coincide with those generated by the reference light.

The electronic arrangement for the measurement system is shown in Fig. 28. Two personal computers are used for the present measurements one of which controls the operation of the CCD camera and receives the images from the CCD camera while the

19

other controls the operation of the laser and the ramp generator of the Fabry-Perot interferometer via an I/O board. So far, preliminary studies have been undertaken which simulate experiments corresponding to various flow velocities are presented. The simulated images are obtained by slowly scanning the Fabry-Perot mirror using the ramp generator and obtaining double exposures on the CCD camera. Each of these images contain a different spacing between the sets of reference and measurement rings, simulating a different velocity.

5.5. Fabry-Perot Images:

Figure 29 shows six Fabry-Perot images captured by the CCD camera, simulating different velocities ranging from zero (Fig. 29-a), to the maximum velocity with the Doppler shift corresponding to nearly the FSR (3.75 GHz) of the system (Fig. 29-f). In Fig. 29-a, only one set of rings is present (corresponding to the reference or zero velocity condition). Note that in the subsequent images, a second set of concentric rings form which move towards the center of the circles. This set of rings represents the Mie scattered light from the probe volume with increasing velocities towards the rightmost image (Fig. 29-f). Finally, in Fig. 29-f, the Doppler shift is almost as large as the FSR and the rings from the measurement volume nearly overlap the reference rings.

5.6. Image Processing for Velocity:

The next objective is to process these images in order to determine the corresponding velocities. Note that each image contains its own reference along with the measurement. Therefore, with a proper image processing scheme, the measured velocities should be independent of small drifts in the alignment of the interferometer and the frequency of the laser.

Software was developed to analyze the images shown in Fig. 29. Again, the objective of the processing is to obtain frequency shift in the measurement signal (and hence the velocity), given an image consisting of two sets of concentric circles (from a single Fabry-Perot) regardless of the position of their center on the CCD surface. All the steps described below are carried out by dedicated software.

As a first step, the center of the circular rings is obtained. Then, the circular rings are mapped, pixel by pixel, onto the r-θ plane through a two-step process as shown in Figs. 30 and 31. The r values of the fringes in Fig. 30 have a minimum for $\theta = \pi/4$ and $3\pi/4$ due to the linear pixel configuration on the CCD camera. This is corrected in Fig. 31 by multiplying the r value for each pixel by an appropriate coefficient in order to obtain r'. Note that, as characteristic of the Fabry-Perot interferometry, the higher order rings have smaller increments in radius. Vaughan (1989)[38] gives the radius relationship between two consecutive rings as

$$R_{p+1} \cong \sqrt{R_p^2 + \frac{2f^2}{n}}$$ (9)

where, R is the radius of ring, p is the fringe number, n is the order of interference and f is the focal length of the fringe forming (or focusing) lens. In the present, a best fit is obtained for the above equation using the actual images as follows:

20

$$R_{p+1} \cong \sqrt{1.05 R_p^2 + 4155} \qquad (10)$$

By using the above equation as a compensation factor, the spacing of the fundamental (or reference) fringes is made constant as shown in Fig. 32-a. Each ring in the Fig. 29 is represented by a straight fringe in Fig. 32 when r′ is transformed into r″. While only the reference fringes exist in Fig. 32-a, the next image to its right has an extra set of rings whose distance to the reference rings characterizes the Doppler shift in the measurement signal. This distance increases with each consecutive image finally in Fig. 32-f, almost coinciding with the original reference fringes.

Several statistical tools, based on correlation functions and Fourier transformations are investigated as possible tools to determine the average distance between the reference and the Doppler shifted fringe in each image of Fig. 32. Figure 33 shows the results of one such method which is based on obtaining the correlation function of the two dimensional image. The correlation coefficient is obtained as follows:

$$R(i) = \frac{\sum\limits_{n=1}^{N-i} I_n I_{n+i}}{\sum\limits_{n=1}^{N} I^2_n} \qquad (11)$$

Here, I_n is the intensity reading for entry n and N is the total number of entries as $N = r''\theta$. The derivative of the correlation function for each case is shown in Fig. 34 in order to better identify the location of individual peaks. Note that in Fig. 34, each zero crossing reaching from the positive side of $R'(r'')$ corresponds to a peak in Fig. 33. The dominant fringe spacings in Fig. 32 are clearly identified in Fig. 34. The correlation function for each case studied clearly shows a peak at $r'' = 51$ which corresponds to the spacing for the FSR. In Fig 33-a, since there is no shift in measured frequency, the only peak is that for the FSR. In case c, however, a second peak is formed at $r'' = 26$ which corresponds to the shift frequency. The picture is more complicated for the subsequent cases since additional complementary peaks appear. This points to the fact that with the present technique, frequency measurements only up to one half of the FRS can be made in order to avoid measurement ambiguity. This is also true for spectral techniques that are currently under investigation.

Again, these results are preliminary. Further studies are being carried out using other image processing techniques. Currently, the MUSIC, Pisarenko, Prony and Maximum Entropy (Berg's Algorithm) techniques are being tested. These methods have been developed for periodic signal detection embedded in noise and their utility in the present application is being investigated. Tests are being carried out with different signal-to-noise levels. Additionally, the processing methods will also be tested in actual velocity measurements using the bench-top supersonic wind tunnel shown in Fig. 27.

VI. Laser Vorticity Probe

In this phase, the concepts for a novel laser-based technique for the measurement of strain rate and vorticity in transparent fluid flows were developed. The technique is based on the collection and direct heterodyning of coherent light scattered from individual seed particles in two adjacent locations and, thereby, allowing the determination of a component of the strain rate tensor. The beat frequency of the heterodyned light, which is proportional to the velocity difference of the two points, is analyzed using a conventional LDA processor. The angle between the laser beam and the direction of the scattered light determines the measured component of velocity. Therefore, a component of the vorticity vector can be measured by using two sets of transmitting and collecting optics, focused at a single location, along with two LDA processors. The basic principle of the technique has been verified through measurements on a thin rotating wire and in a laminar flow between two concentric cylinders with encouraging results. In the latter experiment, the measured velocity differences between two radial locations in the flow agree well with the exact solution.

6.1. _Role of Vorticity in Turbulence Research:_

In order to improve our understanding of complex flow phenomena, advanced non-contact measurement techniques need to be employed that can provide time-resolved, local measurements of the basic turbulent flow characteristics without disturbing the flow field. One such flow characteristics is the vorticity which can provide a wealth of information on the nature of turbulence. The direct measurement of vorticity in a turbulent flow has the advantage of providing basic information on the flow structure and, thus, has been sought by researchers for a long time. The vorticity vector is one of the defining properties of turbulence, whether in development or in equilibrium. The turbulent fluctuations that are superimposed on a mean flow are essentially caused by the vortical motions of various scales and orientations. Vorticity is also the fundamental mechanism responsible for mixing processes and turbulent transport. Direct, time-resolved measurements of vorticity can also help improve our understanding of coherent structures that tend to dominate most shear flows. From code validation point of view, data gathered from direct measurements can provide higher accuracy vorticity data base than those inferred from, say, velocity measurements. Despite these advantages, measurements of vorticity have been much less common than those of velocity among turbulence researchers primarily due to the limitations in the available measurements methods as described in the following section.

The vorticity vector is defined as the curl of the velocity and can be expressed in the tensor notation in Cartesian coordinates as

$$\Omega_i = E_{ijk} \frac{\partial U_k}{\partial x_j} \tag{12}$$

where, E_{ijk} is the alternating tensor and U_k is the velocity vector. Obviously, in order to gain a complete understanding of the instantaneous vorticity field, it is desirable to obtain all three components of the vorticity field simultaneously. However, in most shear flows of practical interest, usually a single component of the vorticity vector is dominant over the other two and tends to control turbulent mixing. For example, large scale coherent

structures in turbulent jets and mixing layers are typically aligned such that they produce the largest vorticity with an axis normal to the main flow direction. Hence, a wealth of information can be gained by the study of this single component.

6.2. Previous Strain-Rate and Vorticity Techniques:

Most of the previously proposed vorticity techniques have been based on physical probes which had varying degrees of obtrusiveness. In an earlier attempt, Zalay (1976)[17] and Wigeland et al. (1977)[18] used a vorticity indicator which is basically a multi-blade vane connected to a shaft which rotated in the direction of vorticity, through a calibration, presumably giving the magnitude of a vorticity component. This method is limited to the measurement of vorticity in the streamwise direction only and it creates a large obstruction in the flow and typically, has poor spatial resolution. Furthermore, since the probe is mechanical, inertia and frictional resistance can cause underestimation of the vorticity magnitude[19]. Another method is based on the measurement of pressures at different yaw angles via multiple-prong pitot tubes as proposed by Freestone (1988)[20]. Although it has the additional capability of measuring vorticity in directions other than streamwise, the technique has a rather poor angle of acceptance for velocity and thus is not very reliable for large vorticity values. In addition, this intrusive method has relatively poor spatial and no temporal resolution.

The most commonly attempted vorticity measurement technique is the one based on thermal anemometry. This method uses multiples of hot-wire sensors to measure velocity components at closely spaced locations in order to obtain the appropriate velocity gradients (or strain rates). The earliest known attempt was made by Kovasznay (1954)[21] who used a four-wire probe to determine the streamwise component of vorticity. The technique was expanded in the following years by several researchers in attempts to improve the accuracy and spatial resolution of the method and to obtain multiple components of the vorticity simultaneously. Foss (1976)[22] developed an array of four wires to measure a single component at a time of the cross-stream components of vorticity. Foss and Haw (1990)[23] later refined the probe design to improve its accuracy and made some measurements in a mixing layer. Klewicki et al. (1992) used the same method in an attempt to study the cross-stream vorticity components in a turbulent boundary layer[23]. Subsequently, several attempts have been made for three-component simultaneous measurements of the vorticity vector using various configurations of clusters of hot-wire sensors including some which used nine independent wires [24-27]. The hot-wire based vorticity techniques are comparatively less intrusive that those discussed earlier, however, the existence of a physical probe in the flow not only disturbs the flow but also makes the system vulnerable in hostile flow environments. Such environments are presented by, for example, combustion flows and high-speed aerodynamics.

In view of these limitations of physical probes, several attempts have been made in order to develop laser-based, non-intrusive vorticity measurement techniques. Lang and Dimotakis (1982)[28] and Lang (1985)[29] used a laser Doppler anemometer (LDA) in order to measure a vorticity component. Driven by an argon-ion laser, the optical system formed a four-spot probe volume and each of the two components of velocity were measured at two locations separated approximately 2 mm from one another. This way, an approximate value of the vorticity component was measured. The technique is quite cumbersome as it

requires appropriately positioned eight distinct the laser beams and collection of Doppler bursts from four probe volumes which are subsequently analyzed by simultaneously using four detectors and LDA counters, all to obtain a single component of the vorticity vector. Agui and Andreopoulos (1994)[30] made certain improvements to this LDA-based method. They reduced the number of laser beams to four by using two elongated probe volumes and collecting signal at two distinct locations in the same long volume. Still, they had to use an argon-ion laser and a set of four detectors and burst spectrum analyzers to obtain the four distinct velocities. Furthermore, the elongation of the probe volume using long focal length transmitting lenses results in large fringe spacings and small numbers of fringes.

Frisch and Webb (1981)[31] proposed a more direct measurement of vorticity components which involves the illumination by a laser light of specially designed and manufactured plastic beads in which, plane mirrors are embedded. The crystal mirrors reflect the laser light and the time that takes for each reflected light to travel a small angle predetermined by two slits is measured and related to vorticity. This method provides an improved spatial resolution, however, several severe requirements limit the application of the technique to most practical flow situations. The specially manufactured beads are relatively large ($\approx$25 μm in diameter) and need to be refraction index matched with the working fluid. Furthermore, the application of this technique is limited to water (and possibly other liquid) flows and does not present much hope for use in gas flows in the future. In another method, a grid of lines are "written" on a plane in the flow by, for example, Raman excitation or laser-induced fluorescence and subsequently imaged to determine the distortion of the grid and relate it to the rate of rotation of the fluid. The drawback of this approach is that it is complicated requiring expensive equipment to obtain limited and only moderately accurate data. The spatial resolution of the techniques in most cases is relatively poor and since a time delay is needed before the interrogated plane is imaged, Taylor's "frozen turbulence" hypothesis has to be invoked. A review of these techniques can be found in Miles (1993)[32].

Particle image velocimetry, (PIV) and holographic PIV have also been used to obtain vorticity [33,34,35]. In recent years, PIV has gained popularity as a planar two-component velocity measurement technique. Once the velocity distribution is obtained, an estimate of a single component of the vorticity can be made from the velocity data. Although this technique is quite powerful as a two-dimensional velocity imaging tool, its application as a vorticity probe has its limitations. First of all, each measurement location is a sub-region of the total image and requires a collection of particles for a valid velocity measurement. This can curtail its ability to provide vorticity measurements sufficiently resolved in space in many applications particularly since at least two adjacent sub-regions need to be used to form each velocity gradient. The need for a large number of particles for each time-frozen measurement and the fact that the laser energy is spread over a large plane results in a signal-to-noise ratio that is inherently smaller than that a single point, single particle technique can provide under similar conditions. In addition, at the present, PIV cannot provide time series vorticity information due to technological limitations in laser pulse rates and image acquisition/analysis speeds.

In this phase of the research work, a new laser-based measurement concept is investigated for the temporally- and spatially-resolved measurement of strain rate and

vorticity, which eliminates a number of the limitations of the current optical probes. As will be described in more detail in the following section, it has the potential to better resolve measurements in both time and space. Unlike all the laser methods listed above, which infer gradients from velocity measurements, the presently proposed technique provides a direct measurement of velocity differences at adjacent locations thereby improving the inherent accuracy of strain rate and vorticity measurements. For each component of vorticity, only four laser beams and two LDA signal processors are needed, significantly reducing the complexity and the cost of measurement. Furthermore, since it depends on the passage of a single particle through each focused laser beam, smaller diameter scatterers and lower CW laser powers can be employed for meaningful measurements.

6.3. Measurement Principle

Laser light scattered from a moving particle will exhibit a Doppler shift that is dependent on the angle between the incident laser beam and the scattering direction as well as the magnitude of the particle velocity. This principle of light scattering is illustrated in Fig. 26 where k_0 and k_s are the wave vectors for the incident laser light and the scattered light, respectively. The scattered light from a particle with a velocity, V, will be Doppler shifted by an amount $\Delta f = (1/2\pi)(k_s - k_0) \cdot V$. With the assumption that the magnitude of the wave vectors is $2\pi/\lambda$, the Doppler shift can be expressed as $\Delta f = (2V_x/\lambda)\sin(\alpha/2)$ where, λ is the incident laser wavelength and V_x is the component of velocity along the direction $(k_s - k_0)$. Therefore, by judicially placing the laser beam and the collecting optics, one can select a component of velocity to measure. By changing α, one can also control the magnitude Δf and optimize it for a given experiment.

In the present technique, scattered light from two closely spaced parallel beams with the same k_0 is collected along a single direction having the same k_s and heterodyned to obtain the difference in Δf which is proportional to the velocity difference along x direction (Fig.26). The coherent, Mie scattered light from two individual particles are captured using a single lens and combined into a single colinear beam. Subsequently, the beam is focused onto the surface of a photodetector where the beat frequency is generated. In order to obtain a beat frequency at the sensor surface, the tolerance on the angel of divergence between the two beams has to be very small. After trying several different methods, it was determined that a relatively easy way to combine the signal from the two individual particles into a single colinear beam is to couple them both into a single mode optical fiber. When the output of the fiber is shone on a photodetector, the signal from it will contain the beat frequency. This frequency carries the velocity difference information and is analyzed by an LDA signal processor. Since the distance between the two laser beams is known, the strain rate, $\Delta U_i/\Delta x_j$, can easily be calculated. In order to overcome the ambiguity in the sign of the derivative, one of the beams is frequency shifted by passing it through a Bragg cell.

Figure 35 shows the basic optical configuration for the measurement of the vorticity component along z direction. The laser beams and the collection direction that lie on the x-z plane, (denoted by subscript 1) measure $\partial U/\partial y$. Note that $k_{0,1}$ represent two parallel laser beams, one of which is 40 MHz frequency shifted and slightly separated from the

25

other in y direction. Similarly, the laser beams and collecting direction that lie on the y-z plane (denoted by subscript 2) measure $\partial V/\partial x$. Again, one of the two laser beams represented by $k_{0,1}$ is frequency shifted by a Bragg cell and is separated from the other in the x direction by a small but adjustable amount. Together, $\partial U/\partial y$ and $\partial V/\partial x$ form the vorticity component Ω_z.

6.4. Optical Setup

Figure 36 shows the details of the transmitting and collecting optics for each of the planes. The beam from a 10 mWatt helium-neon laser is first passed through a Bragg cell. The unshifted and the 40 MHz frequency-shifted beams are passed through an iris diaphragm discarding all other higher order beams. An achromatic, long focal length lens brings the two beams close together at the measurement area (probe volume). The beams are nearly parallel and the distance between the two beams can be adjusted as desired. One set of achromatic lenses collect and refocus the scattered light from individual particles on the plane of twin pinholes. The focusing lens has a longer focal length than that of the collimating lens providing a larger spacing between the pinholes than that between the two laser beams at the probe. The set of two lights are separated by a prism as shown and collimated with an approximate diameter of 1 mm and fed into the mini GRIN lenses that are attached to the ends of the single mode fiber (approximately 3.5 μm core diameter). A built-in beam combiner, with 50% efficiency combines the two signals which ensures a perfect colinearity and preserves the coherence of the scattered light. The output of the fiber which is also fitted by a mini GRIN lens and produces a collimated light. This output is focused onto the surface of a photomultiplier tube and the beat frequency is observed by a LDA counter. The output signal of the counter from each plane (illustrated in Fig. 35) is fed into a personal computer where the real-time calculation of the vorticity is carried out.

An optical system, similar to that shown in Fig 36, has been developed and two sets of experiments have been carried out to test the proposed technique. In the first of these, the concept of using direct heterodyning to obtain $\Delta U/\Delta y$ has been tested with excellent results. This was accomplished by measuring velocity difference at two radial positions on a rotating wheel. In the second set of experiments, velocity difference at two radial locations in a laminar flow between two concentric cylinders was measured using the new technique.

6.5. Rotating Wheel Measurements

A Plexiglas wheel with a 50 μm copper wire running along its radius is placed in the optical probe volume. As described earlier, a 10 mWatt He-Ne laser drives the optical system. This is an off-the-shelf laser with no special modification such as temperature stabilization. The optics are aligned with the wheel at rest and the two laser beams illuminating the wire at two locations. The separation distance between the two laser beams at the probe is $\Delta y = 1.2$ mm. One of the beams is 40 MHz frequency shifted using a Bragg cell. Therefore, when the wheel is at rest a 40 MHz modulation is observed at the output of the PMT. (In these experiments, a system of beam splitters are used in place of the optical fiber in order to combine the scattered light from the two spots). As the wheel spins at different angular speeds, the frequency increases or decreases depending on the rotational direction of the wheel. A sample oscilloscope trace of the high-pass filtered

PMT output is shown in Fig.37. As the wire sweeps past the optical probe, an enveloped beat frequency is clearly detected which resembles the Doppler burst in an LDA measurement. The output of the PMT is fed into an LDA counter and the tangential velocity difference of the two spots along the wheel radius separated by Δy is measured for a range of wheel rotational speeds. The signal from the PMT is first passed through a downmix circuit to reduce the original Bragg cell frequency in order to optimize it for analysis on the counter. The results are shown in Fig. 38. The rpm of the wheel is measured independently and the tangential velocity differences are calculated from this in order to provide an independent comparison. The velocity difference (ΔV) values on the abscissa of Fig. 38 are calculated from:

$$\Delta V = \frac{2\pi (rpm)\Delta y}{60} \tag{13}$$

The measured and calculated velocity differences are in excellent agreement providing the first confirmation of the proposed method. The negative ΔV values are obtained by reversing the rotational direction of the wheel. The system is equally effective in determining ΔV in both directions.

6.6. Measurements in Laminar Flow

Measurements were also performed in a laminar flow of water between two concentric cylinders. The difference in circumferential velocity at two radial locations in the flow were obtained using the optical system shown in Fig. 36. In order to achieve a stable momentum stratification and thus a large range of Reynolds numbers in the laminar flow regime, the inner cylinder was kept stationary while the rotational speed of the outer cylinder was varied. As shown in Fig. 39, the experimental facility is a water tank with the concentric cylinder system placed inside it. The inner cylinder is a solid aluminum bar while the outer cylinder is a glass tube. The outer cylinder is controlled by a variable speed DC motor via a belt drive system. The inner and outer cylinder radii are r_i=14 mm and r_0=24 mm, respectively. The total length of the cylinders is L=205 mm. The resulting cylinder length-to-gap-width ratio is [L/(r_0-r_i)]=20.5 which is large enough to allow a two-dimensional (axisymmetric) flow away from the cylinder ends. Therefore, the only the circumferential velocity component exists.

The two laser beams enter the tank from the bottom and pass through one side of the cylinder system as shown in Fig 39. Here, k_s is the direction along which the scattered light is collected. The receiving optics are situated such that the scattered light is collected at two points on the horizontal radius of the cylinders, and they are separated by Δy=2 mm. Referring to Fig. 26, one sees that the measured velocity is 45 deg. out of the plane of motion. However, the flow is purely circumferential and the measured component is related to this velocity by the (Cos 45) factor. The water in the tank is prefiltered to remove unwanted particulates. The region of flow to be interrogated is then seeded by silver-coated hollow glass beads with a nominal diameter of 14 μm.

Figure 40 shows the measured circumferential velocity differences for a range of outer cylinder rotational speeds. The optical probe is located at r=1.9 mm. The probe location is defined as the mid-point of the two measurement spots (with r_i=1.8 mm and r_2=2 mm). From the exact solution to the problem of viscous circumferential flow

between two concentric cylinders with inner cylinder at rest, the velocity difference between two spots with radii r_1 and r_2 can be expressed as

$$\Delta V = (V_2 - V_1) = \frac{r_o^2 \omega}{r_o^2 - r_i^2}\left[\left(r_2 - \frac{r_i^2}{r_2}\right) - \left(r_1 - \frac{r_i^2}{r_1}\right)\right] \qquad (14)$$

where, ω is the rotational speed of the outer cylinder and r_i and r_o are the inner and outer cylinder diameters, respectively. The close agreement between the experiments and the exact solution is very encouraging for the proposed measurement technique. First of all, the linear trend of ΔV is very well captured by the measurements which show little scatter in the data. The quantitative agreement between the solution and the measurements is also quite good considering that there is only a small positive bias in the measured data. This measurement bias is most likely caused by the uncertainty in the positioning of the two laser beams relative to one another and to the walls of the cylinder system. Since this is a preliminary study to investigate the viability of the proposed technique, no elaborate positioning methods have been used and the measurement error in ΔV is estimated to be in the order of the bias seen in Fig. 40.

VII. Conclusions

7.1. Dual-Line Detection Rayleigh Scattering:

In single-shot measurements, the calculated shot noise uncertainty in the pressure is higher for the DLDR technique compared to single-line detection. However, single-shot measurement uncertainties of the present system are much better than those of the previous copper-vapor laser based system. In the presence of high levels of background, the best and the worst measurement accuracies are obtained by the DLDR and green line-only systems, respectively. The UV line-only results are relatively close to those of the DLDR technique. This is due to the fact that the UV Rayleigh scattering cross-section is 16 times larger, while the surface scattering is only half that of green, as determined from system calibrations. The combined effect is that the UV signal-to-background noise ratio is over 30 times larger than that of the green. Therefore, using the UV line only is in itself an improvement over using the green line alone. Further pressure tests showed that the DLDR technique works robustly up to a level where the background-to-signal level on the green line is approximately 3. At this level of background contamination, the UV background-to-signal ratio is about 0.1. Therefore, the DLDR method still provides a significant improvement over UV-only measurements. Single-shot temperature measurements were made in an axisymmetric heated air jet using both the single-line detection and the DLDR methods. The mean and turbulent temperature profiles obtained seven diameters from the jet exit are in excellent agreement with those of a fast response thermistor.

7.2. Filtered UV Rayleigh Scattering:

Experiments were carried out to study the possibility of using filtered Rayleigh or Mie scattering in the 266 nm uv line of the Nd:YAG laser. The effort concentrated in the testing of a large number of benzene derivatives and toluenes (given in Table 4). Although some of the material exhibited strong absorption characteristics at the 266 nm line, the tests failed to identify sharp absorption lines in any of the materials considered. Further work may be considered to test several other chemicals listed in Table 3.

7.3. Image Processing for Interferometric Velocimetry:

In this ongoing research effort, image processing methods have been developed to determine, fast and accurately, the Doppler shift in the Fabry-Perot interference patterns obtained using Rayleigh or Mie scattering. The end goal is to obtain on-line time frozen velocity data in high-speed flows using interferometric measurements. The method will also be extended to simultaneous velocity and temperature measurements in the future. In the present stage, the image is first mapped onto a coordinate system where the original "bullseye" pattern is a set of straight lines. Next, either spectral or correlation analysis is carried out to determine not only the FSR but also the Doppler frequency shift due to velocity. The correlation technique, in particular, is promising. The derivatives of the correlation functions identify the FSR as well as the shifted frequency reasonably well. However, it is also noted that with both the correlation and spectral methods, the range of measurable frequency (velocity) is limited to one half of the FSR at the upper end rather

than the full FSR. Therefore, for a given measurement resolution, the dynamic range is one half of what it would have been for a manual, post processing.

7.4. *Laser Vorticity Probe:*

A novel laser-based strain rate measurement technique is presented which can be extended to include vorticity measurements. The proposed technique is straightforward and relatively inexpensive. It affords non-intrusive, accurate, dynamic measurement of strain rate and vorticity in both low-speed incompressible and high-speed compressible turbulent flows. The good agreement between the experimental results and the exact solution clearly indicate that the technique is viable at least as a strain rate measurement method.

Although the principle and setup of the present technique is straightforward, certain considerations related to particle statistics need to be taken into account for successful operation. In order to measure the velocity difference at two locations, a particle should occur simultaneously at each probe formed by the two laser beams so that a signal with a beat frequency is realized. On the other hand, occurrence of too many particles at a time in each probe volume will tend to corrupt the coherent nature of the collected light which will lead to poor light heterodyne. Therefore, particle concentration plays an important role in both the quality and the rate of data. Another consideration is the duration of the particles in the probe region. As the particles are swept through the probe volume by the mean convective velocity, their duration within this volume should be long enough to generate several cycles of the beat frequency so that it can be detected and timed by the signal processing unit. When using the technique for vorticity, a coincidence window can be prescribed such that as long as the two strain rate measurements fall within this certain time duration, the measurement can be considered simultaneous. The selection of this coincidence window will depend on several flow characteristics including turbulence.

VIII. References

[1]Bill, R.G. Jr., Namer, I., Talbot, L., and Robben, F., "Density Fluctuations of Flame in Grid Induced Turbulence," Combustion and Flame, Vol. 44, 1982, pp. 277-285.

[2]Gouldin, F.C., and Halthorne, R.N., "Rayleigh Scattering for Density Measurements in Premixed Flames," Experiments in Fluids, Vol. 4, No. 3, 1986, pp. 269-278.

[3]Dibble, R.W, and Hollenbach, R.H., "Laser Rayleigh Thermometry in Turbulent Flows," Proceedings of the Eighteenth Symposium on Combustion, The Combustion Institute, Pittsburgh, PA, 1981, pp. 1489-1499.

[4]Namer, I., and Schefer, R.W., "Error Estimates for Rayleigh Scattering Density and Temperature Measurements," Experiments in Fluids, Vol. 3, No. 1, 1985, pp. 1-9.

[5]Graham, S.C., Grant, A.J., and Jones, "Transient Molecular Concentration Measurements in Turbulent Jets," AIAA Journal, Vol.12, No. 8, 1974, pp. 1140-1143.

[6]Dyer, T.M., "Rayleigh Scattering Measurements of Time-Resolved Concentration in a Turbulent Propane Jet, " AIAA Journal, Vol. 17, No.8, 1979, pp. 912-914.

[7]Pitts, W.M., and Kashiwagi, T, "The Application of Laser-Induced Rayleigh Scattering to the Study of Turbulence Mixing," Journal of Fluid Mechanics, Vol 141, April 1984, pp. 391-429.

[8]Arcoumanis, C., "A Laser Rayleigh Scattering System for Scalar Transport Studies," Experiments in Fluids, Vol.3, No.2, 1985, pp.103-108.

[9]Ötügen, M.V., and Namer, I., "Rayleigh Scattering Temperature Measurements in a Plane Turbulent Air Jet," Experiments in Fluids, Vol. 6, No. 7, 1988, pp. 461-466.

[10]Miles, R., and Lempert, W., "Two-Dimensional Measurement of Density, Velocity, and Temperature in Turbulent High-Speed Air Flows by UV Rayleigh Scattering", Appl. Phys. Vol. B15, 1990, pp.1-7.

[11]Miles , R B., Lempert, W. R., and Forkey, J. "Instantaneous Velocity Fields and Background Suppression by Filtered Rayleigh Scattering", AIAA Paper 91-0357, January 1991.

[12]Seasholtz, R.G., and Zupank, F.J., "Spectrally Resolved Rayleigh Scattering Diagnostics for Hydrogen-Oxygen Rocket Plume," Journal of Propulsion and Power," Vol. 8, No.5, 1992, pp. 935-942.

[13]Elliot, G.S., Samimy, M. and Arnette, S.A., "Details of a Molecular Filter-Based Velocimetry Technique", AIAA Paper 94-0490, January 1990.

[14]Kouros, H. and Seasholtz, R.G., "Fabry-Perot Interferometer Measurements of Static Temperature and Velocity for ASTOVL Model Tests", *Proc. Symposium on Laser Anemometry: Advances and Applications*, Ed: Huang and Otugen, ASME FED-Vol.191, 1994

[15]Ötügen, M.V., Annen, K.D., and Seasholtz, R.G., "Gas Temperature Measurements Using a Dual-Line Detection Rayleigh Scattering Technique," AIAA Journal, Vol. 31, No. 11, 1993, pp. 2098-2104.

[16]Forkey, J.N., "Development and Demonstration of Filtered Rayleigh Scattering Laser Based Flow Diagnostics For Planar Measurement of Velocity, Temperature, and Pressure", Ph.D. Thesis, Department of Mechanical and Aerospace Engineering, Princeton University, 1996.

[17]Zalay, A.D. 1976 Hot-Wire and Vorticity Meter Wake Vortex Surveys *AIAA Journal* **14** 694

[18]Wigeland, R.A., Ahmed, M. and Nagib, H.1977 Vorticity Measurements Using Calibrated Vane-Vorticity Indicators and Comparison with X-Wire Data", Presented at the 10th AIAA Fluid and Plasma Dynamics Conference, Albuquerque, NM, June 27-29, 1977.

[19]Huachen, P. and Shiying, Z. 1987 Measurement of Streamwise Vorticity Using a Vane Vorticity Meter *Heat and Fluid Flow* **8** 72

[20]Freestone, M.M. 1988 Vorticity Measurement by a Pressure Probe *Aeronautical Journal* **21** 29

[21]Kovasznay, L.S.G. 1954 Turbulence Measurement *High Speed Aerodynamics and Jet Propulsion* (Ed. R.W. Landenbuerg, B. Lewis, R.N. Pease and H.S. Taylor) **9** 213

[22]Foss, J.F. 1976 Accuracy and Uncertainty of Transverse Vorticity Measurements *Bull. Am. Phys. Soc.* **21** 1237.

[23]Foss, J.F. and Haw, R.C. 1990 Vorticity and Velocity Measurements in a 2:1 Mixing Layer *Forum on Turbulent Flows*. (Ed. W. W. Bowers and M. Samimy) ASME-FED **94** 115

[24]Klewicki, J.C., Falco, R.E. and Foss, J.F. 1992 Some Characteristics of the Vortical Motions in the Outer Region of Turbulent Boundary Layers *J. Fluids Engineering* **114** 530

32

[25]Wassman W.W. and Wallace, J.M.1979 Measurement of Vorticity in Turbulent Shear Flows *Bull. Am. Phys. Soc.* **24** 1142

[26]Andreopoulos, Y. and Honkan, A., 1996 Experimental Techniques for Highly-Resolved Measurements of Rotation, Strain and Dissipation-Rate Tensors in Turbulent Flows *Measurement Science & Technology* **7** 1

[27]Vukoslavcevic, P., Wallace, J.M. and Balint, J-L. 1991 The Velocity and Vorticity Vector Fields of a Turbulent Boundary Layer, Part I. Simultaneous Measurement by Hot-Wire Anemometry *J. Fluid Mech.* **228** 25

[28]Lang, D.B. and Dimotakis, P. 1992 Measuring Vorticity Using Laser Doppler Velocimetry *Bull. AM. Phys. Soc.* **27** 1166

[29]Lang, D.B. 1985 Laser Doppler Velocity and Vorticity Measurements in Turbulent Shear Layers Ph.D. Thesis, California Inst. Technology, Pasadena, CA., USA

[30]Agui, H.A. and Andreopoulos, Y. 1994 Development of a New Laser Vorticity Probe-LAVOR *Laser Anemometry: Advances and Applications* (Ed. Huang, T.T. and Otugen, M.V.) ASME-FED **191** 15.

[31]Frisch, M.B. and Webb, W.W., "Direct Measurement of Vorticity by Optical Probe" J. Fluid Mech., Vol. 107, 1981.

[32]Miles, R.B. 1993 Shedding Light on Turbulence *Bull. Am. Phys. Soc.* **38** 2257.

[33]Adrian, R.J.1991 Particle Imaging Techniques for Fluid Mechanics *Annual Review of Fluid Mechanics* **20** 261

[34]Barnhard, D.H., Adrian, R.J. and Papen, G.C. 1994 Phase Conjugate Holographic System for High Resolution Particle Image Velocimetry *Appl. Optics* **33** 7159

[35]Meng, H. and Hussain, F. 1995 Instantaneous Flow Field in an Unstable Vortex Ring Measured by Holographic Particle Velocimetry *Phys. Fluids* **7** 9

[36]Seasholtz, R.G., A.E. Buggele and M. Reeder "Instantaneous Measurements in a Supersonic Wind Tunnel Using Spectrally Resolved Rayleigh Scattering" Proc. International Symposium on Optical Science, Engineering and Instrumentation, San Diego, CA, July 9-14, 1995

[37]Seasholtz, R.G., "Single-Shot Spectrally Resolved UV Rayleigh Scattering Measurements in High Speed Flows", Eighth International Symposium on Applications of Laser Techniques to Fluid Mechanics, Lisbon, Portugal July 8-11, 1996.

[38]J.M. Vaughan, "The Fabry-Perot Interferometer, History, Theory, Practice and Applications", Adam Hilger, Bristol, 1989

[39]C.A. Bunting, P.G. Carolan, M.J. Forrest, P.G. Noonan and A.C. Sharpe "CCD Camera As a Multichannel Analyzer for the Spectral and Azimuthal Resolution of Fabry-Perot Fringes", 1988, Rev. Sci. Instrum. Vol. 59, No. 8, pp.1488-1490.

Table 1: Summary of temperature calibrations for the DLDR system

	C_1 (x10-6) [m-sr]	C_2 (x10-5) [m-sr]	β
Average value	1.365	1.354	2.15
Standard deviation	0.047	0.04	0.11
Percent deviation	3.44	2.95	5.1

Table 2: Summary of pressure calibrations for the DLDR system

	C_1 (x10-6) [m-sr]	C_2 (x10-5) [m-sr]	β
Average value	1.387	1.379	2.07
Standard deviation	0.051	0.044	0.1
Percent deviation	3.68	3.19	4.8

Table 3: Chemicals Considered for as UV absorption filter

Chemical	melting point	boiling point	comments
benzene	5.5	80	highly flammable
chlorobenzene	-45	131.2	
bromobenzene	-30.6	156.2	
fluorobenzene	-40	84.7	
toluene	-95	110.6	flammable
2-fluorotoluene	-62	114	
3-fluorotoluene	-87.7	116	
4-fluorotoluene	-56.8	116.6	
2-chlorotoluene	-35.1	159.1	
3-chlorotoluene	-47.8	162	
4-chlorotoluene	7.5	162	
2-bromotoluene	-27.8	181.7	
3-bromotoluene	-39.8	183.7	
4-bromotoluene	28.5	184.3	
aniline	-6	184-6	colorless, poison
4-fluoroaniline	-1.9	188	
3-fluoroaniline	-	187	
2-fluoroanilin	-28.5	174-6	
4-chloroaniline	72.5	232	
3-chloroaniline	-10.3	229.9	
2-chloroaniline	-14	208.8	
4-bromoaniline	66.4	d	
3-bromoaniline	18.4	251	
2-bromoaniline	32	229	
naphtalene	80.5	218	
alphamethylnaphtalene	-22	244.6	
betamethylnaphtalene	34.6	241	
alphabromonaphtalene	-6.2	281	
betabromonaphtalene	2-3	281	
alphachloronaphtalene	-2.3	258.8	
betachloronaphtalene	61	256	
alphafluoronaphtalene	-9	215	
betafluoronaphtalene	61	211.5	
SO_2	-72.7	-10	toxic, corrosive
CH_2	-92	-21	formaltehyde
CO_2			carbondioxide
CO	-199	-191	c-monoxide
S_2	112.8	445	
F_2	-216.6	-188	corrosive, very reactive

Table 4: Chemicals tested for UV filter

Toluene
2-fluorotoluene
3-fluorotoluene
4-fluorotoluene
benzene
bromobenzene
fluorobenzene
monochlorobenzene

IX. List of Figures

Fig. 1: Optical setup for the DLDR system

KEY

A	Pinhole	M	Mirror
B.D.	Beam dump	P	Probe
B.S.	Beam splitter	P.B.R.	Wave Plate
H.G.	Harmonic generator	P.D.	Photo diode
H.S.	Harmonic separator	PMT	Photomultiplier tube
L	Lens		

Fig. 2: Electronic arrangement for the DLDR system

BEAM DUMP

BEAM DUMP

HOT AIRJET

ARCHROMAT
LENS

BLACK BOX

X

Y

COLLECTING
LENS

BLACK BOX
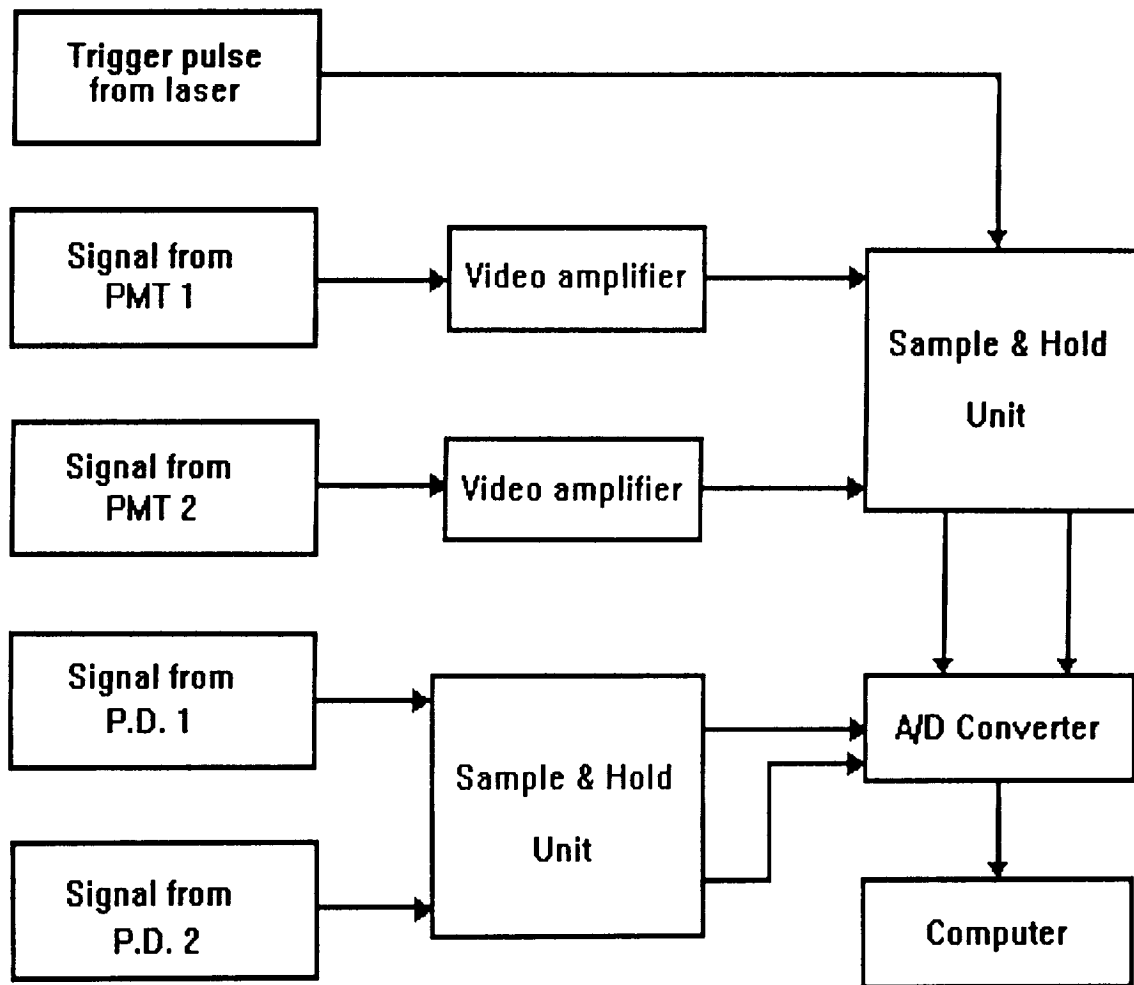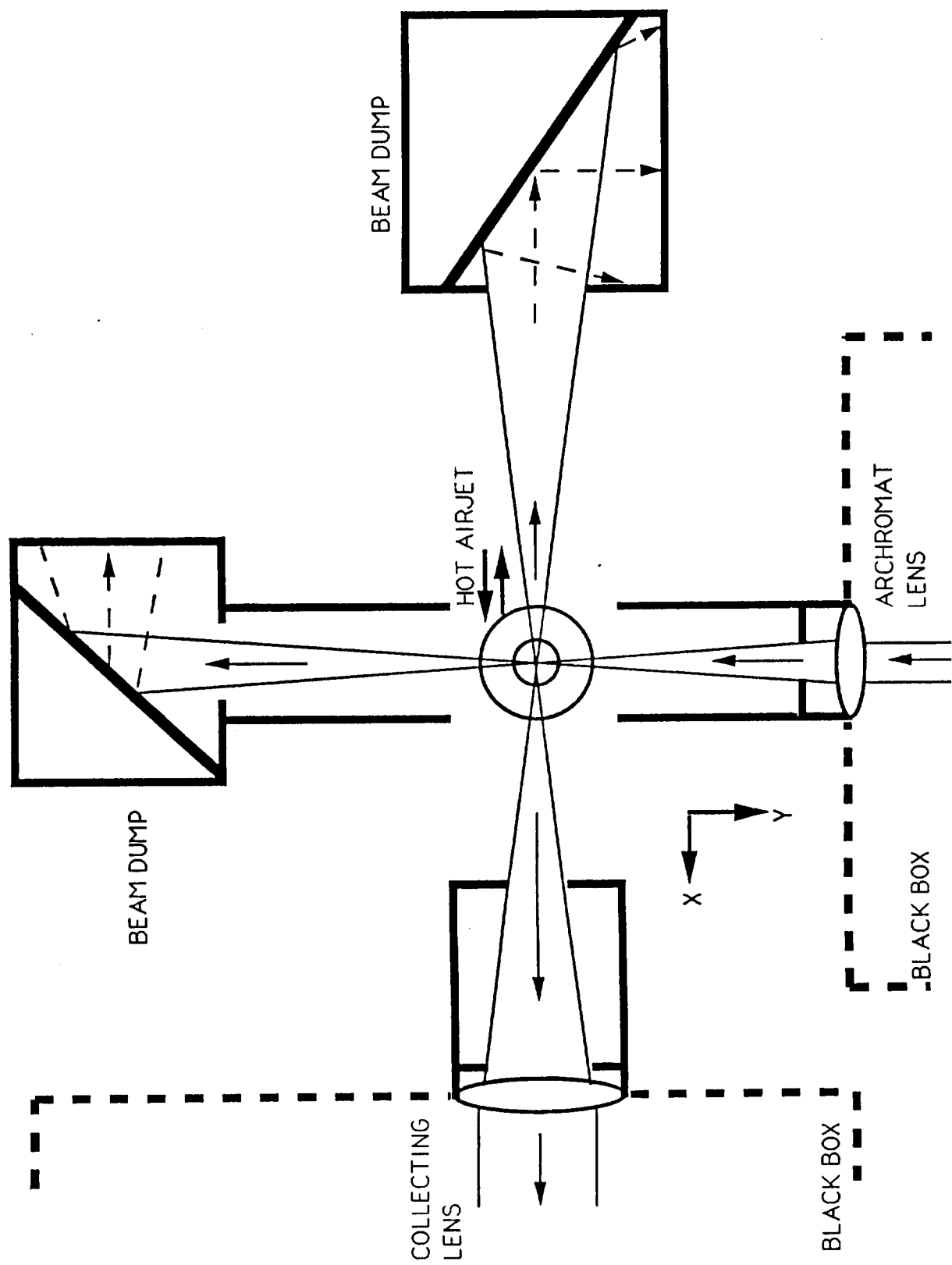
Fig. 3: Jet calibration setup with DLDR optical probe
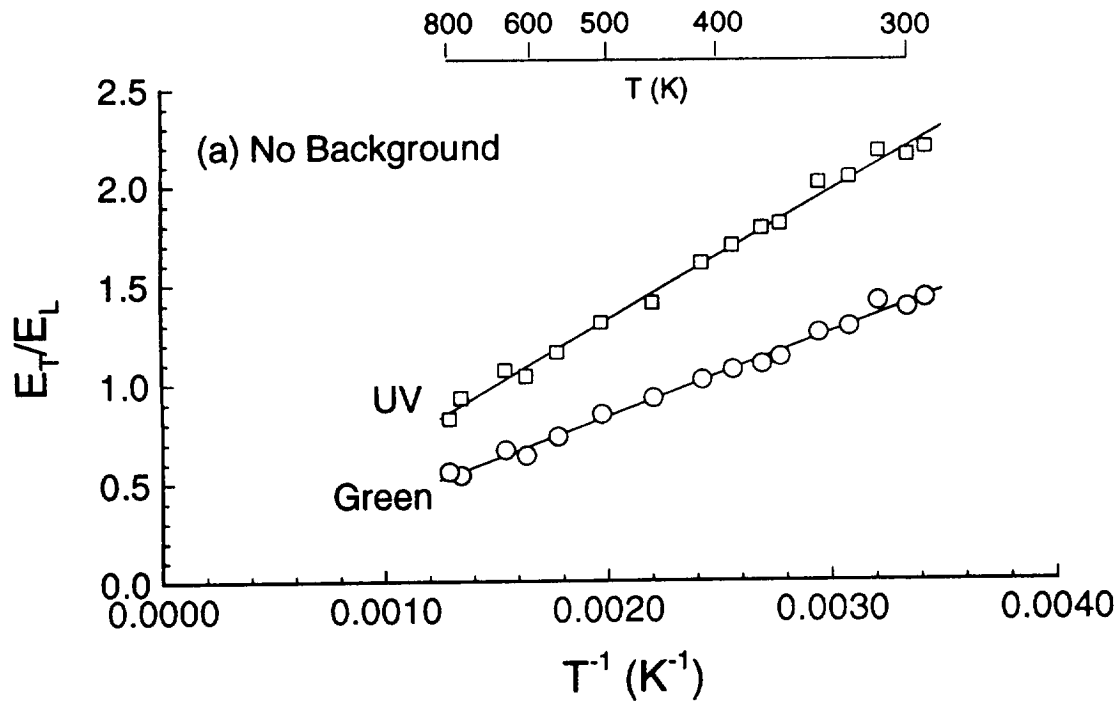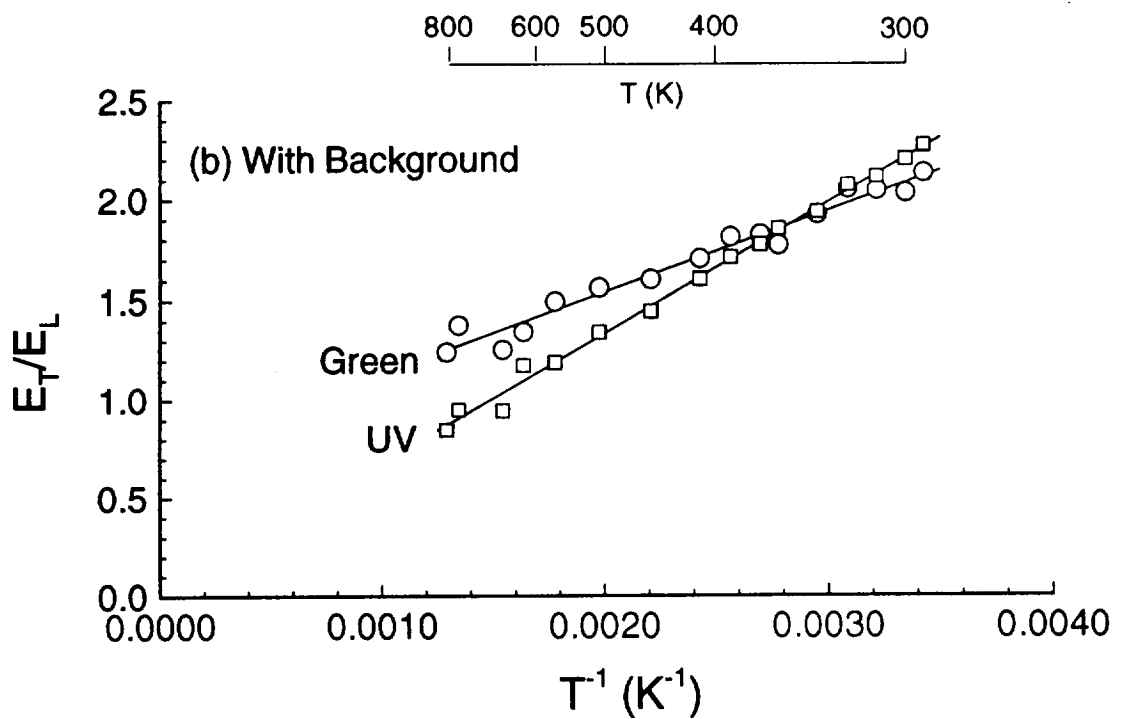
Fig. 4: Jet calibrations (a) without background; (b) with background contamination
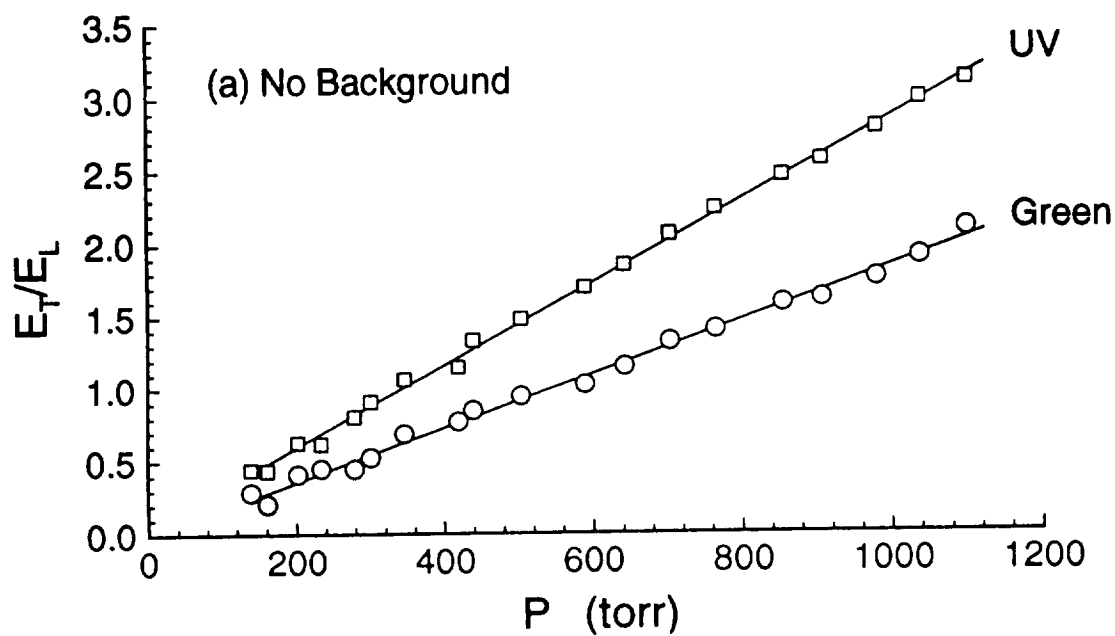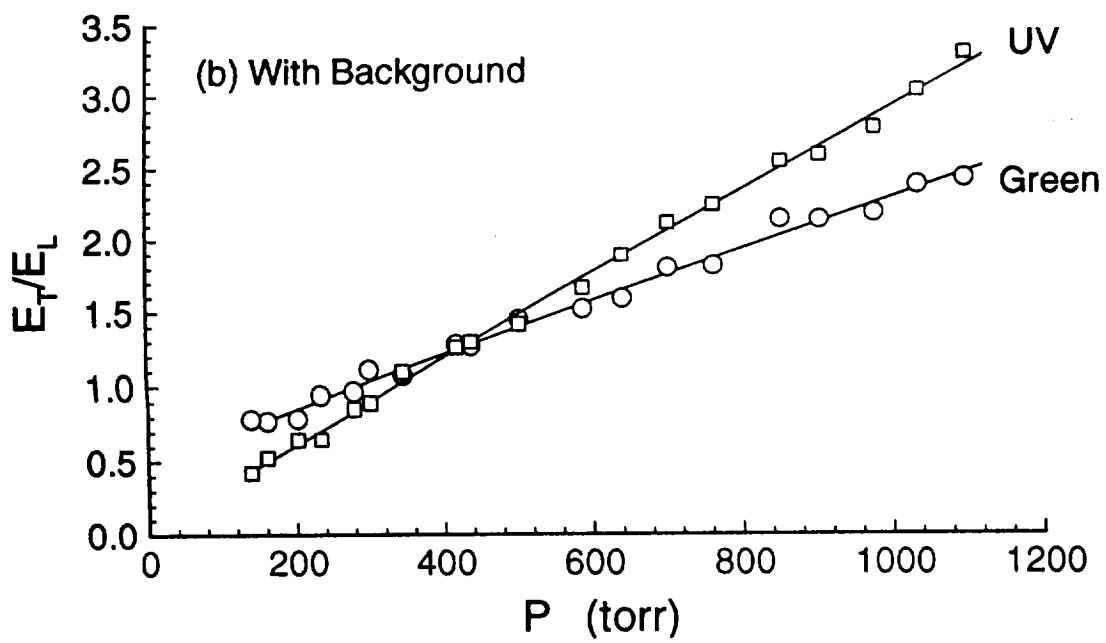
Fig. 5: Vacuum chamber calibrations (a) no background; (b) with background contamination
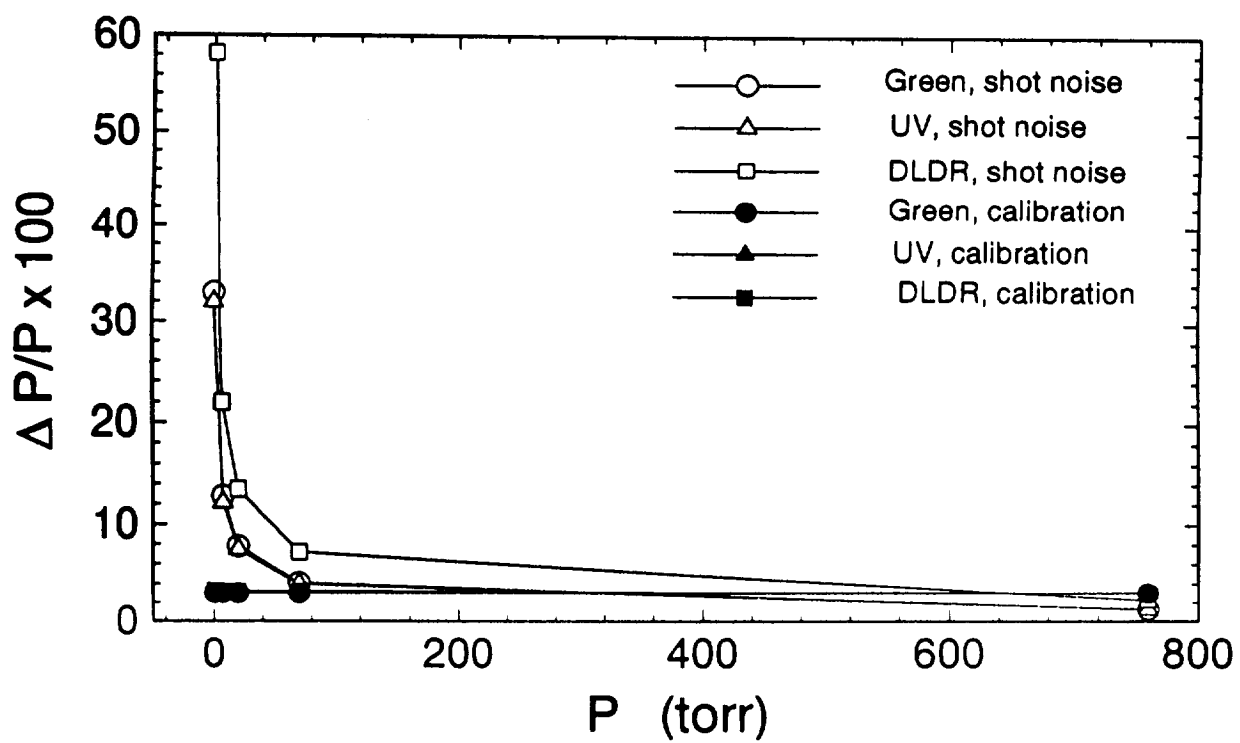
Fig. 6: Error estimates for vacuum pressure measurements
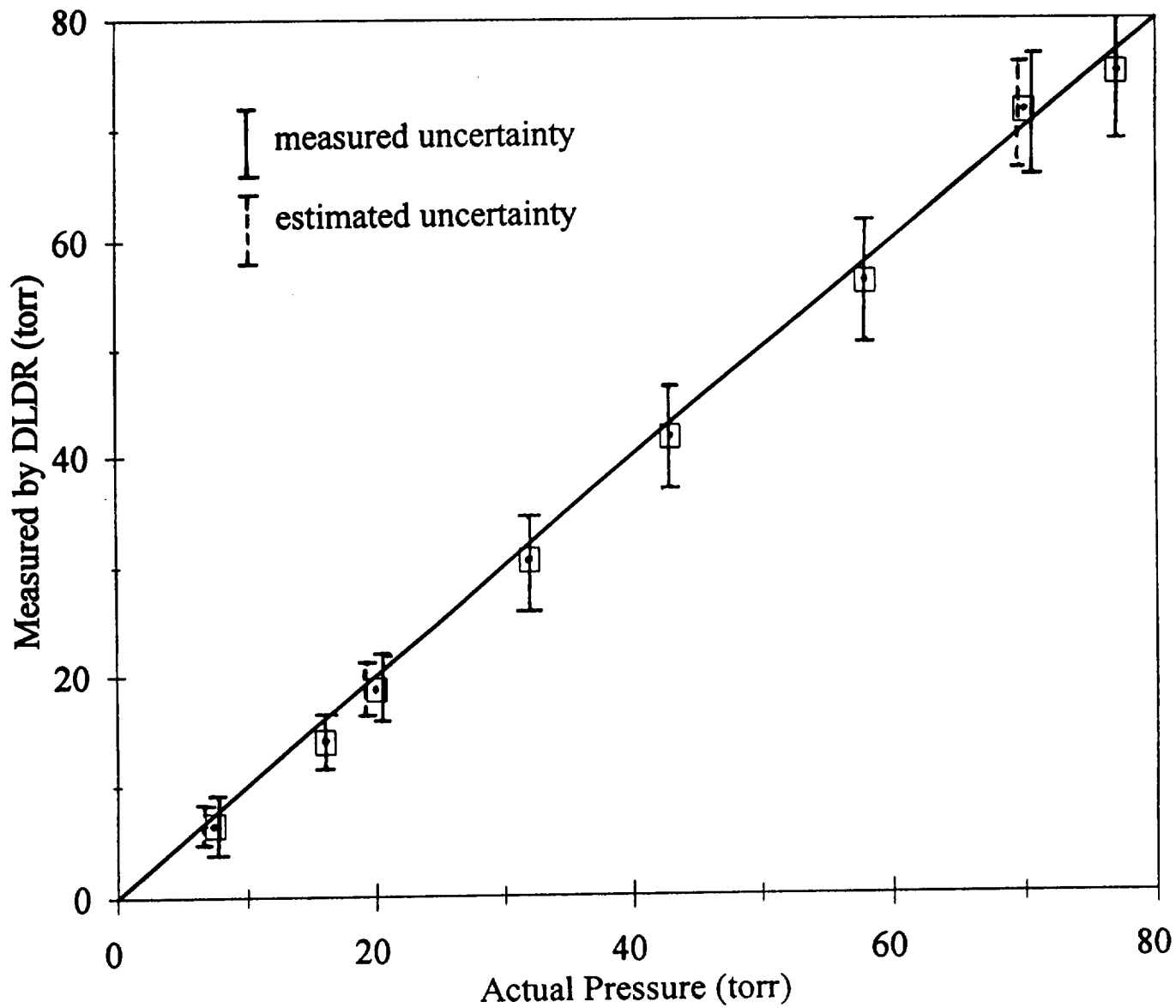
Fig. 7: Vacuum pressure measurements using the DLDR system
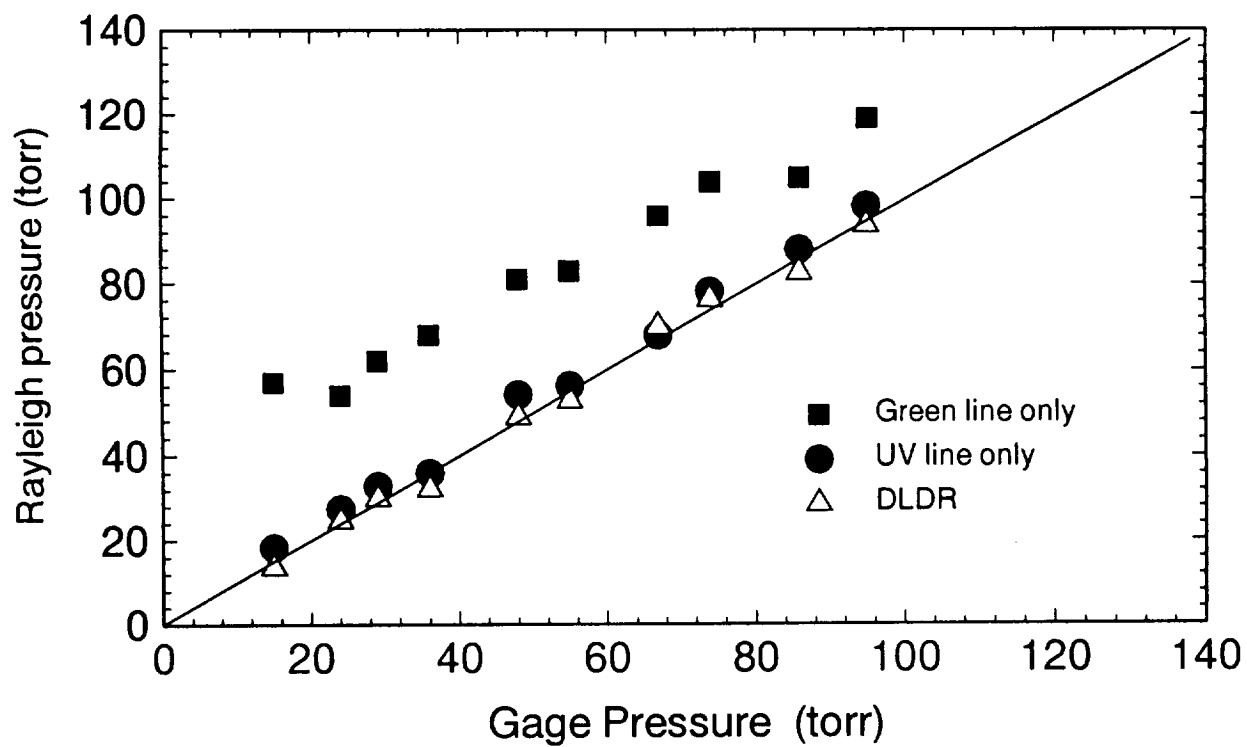
Fig. 8: Comparison of single line and DLDR pressure measurements
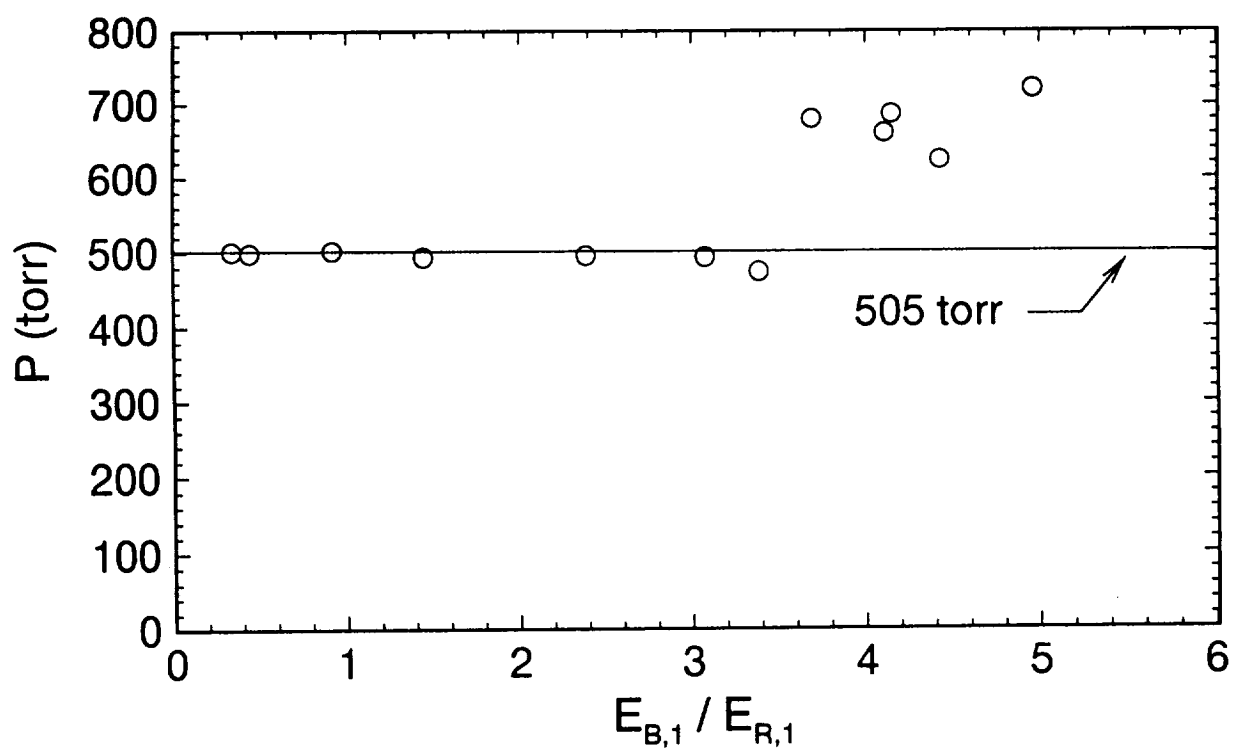
Fig. 9: Effect of background level on DLDR measurements
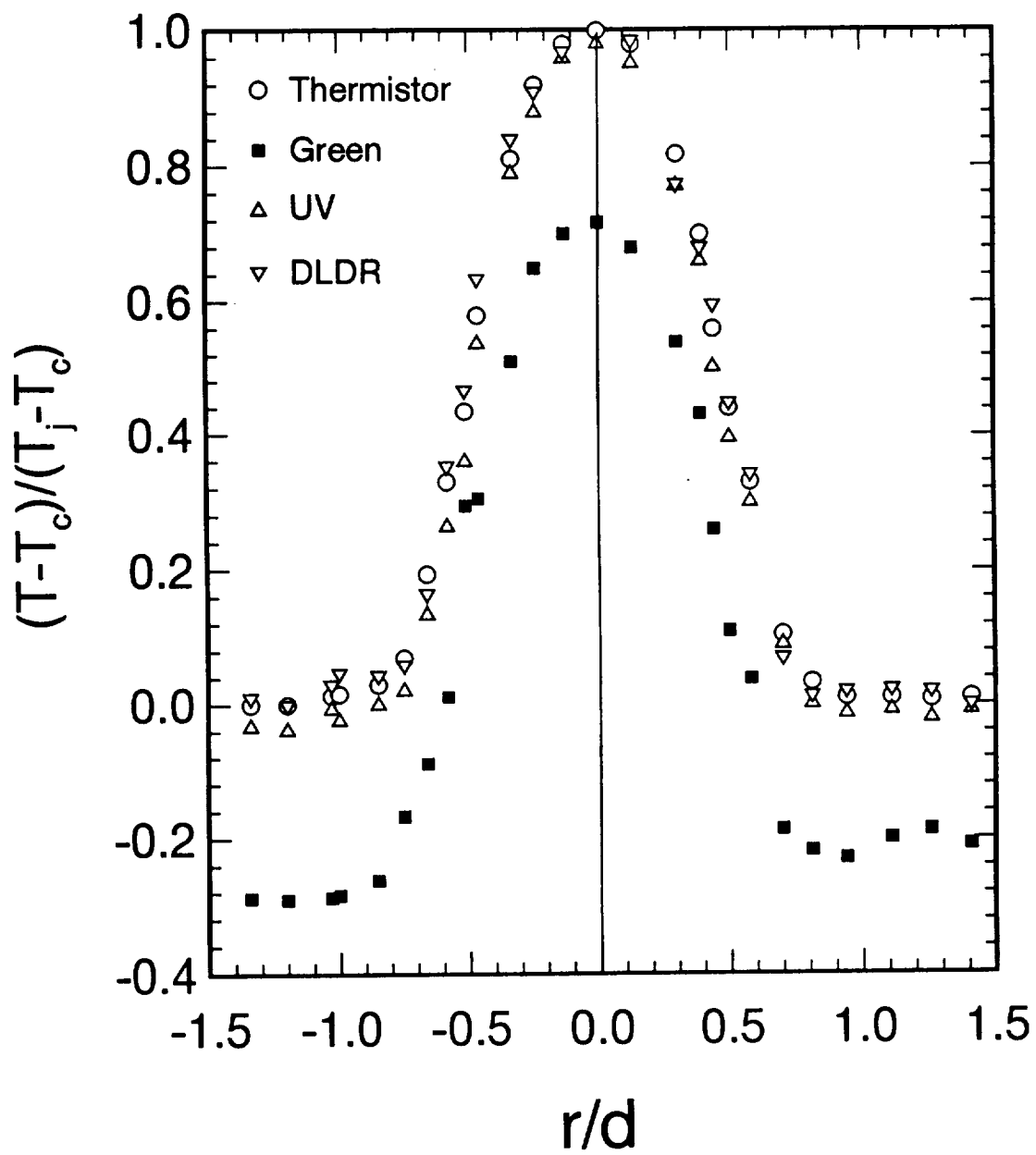
Fig. 10: Mean temperature profiles in heated jet; x/d=7
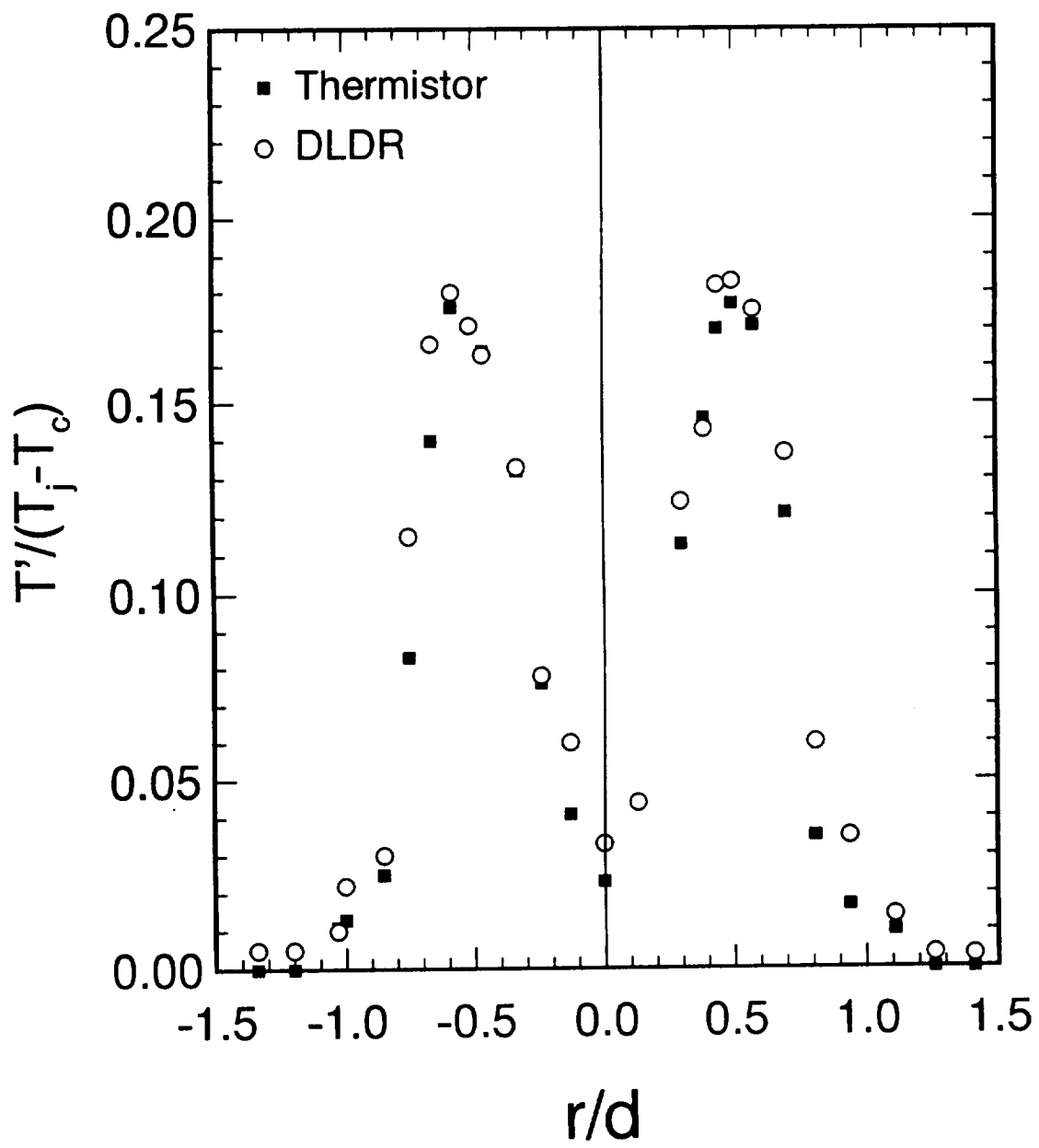
Fig. 11: RMS of temperature fluctuations in heated jet; x/d=7
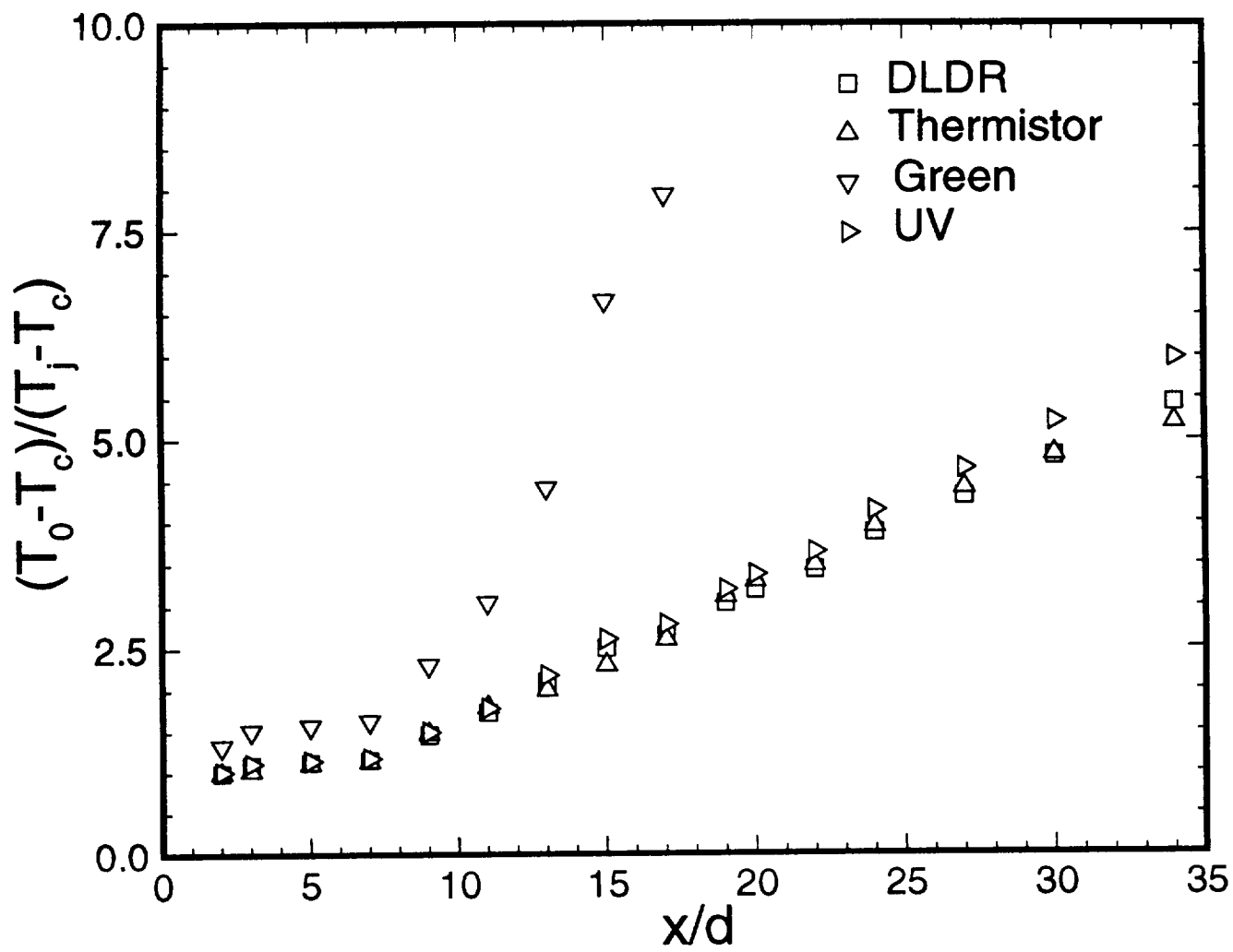
Fig. 12: Jet mean centerline temperature distribution
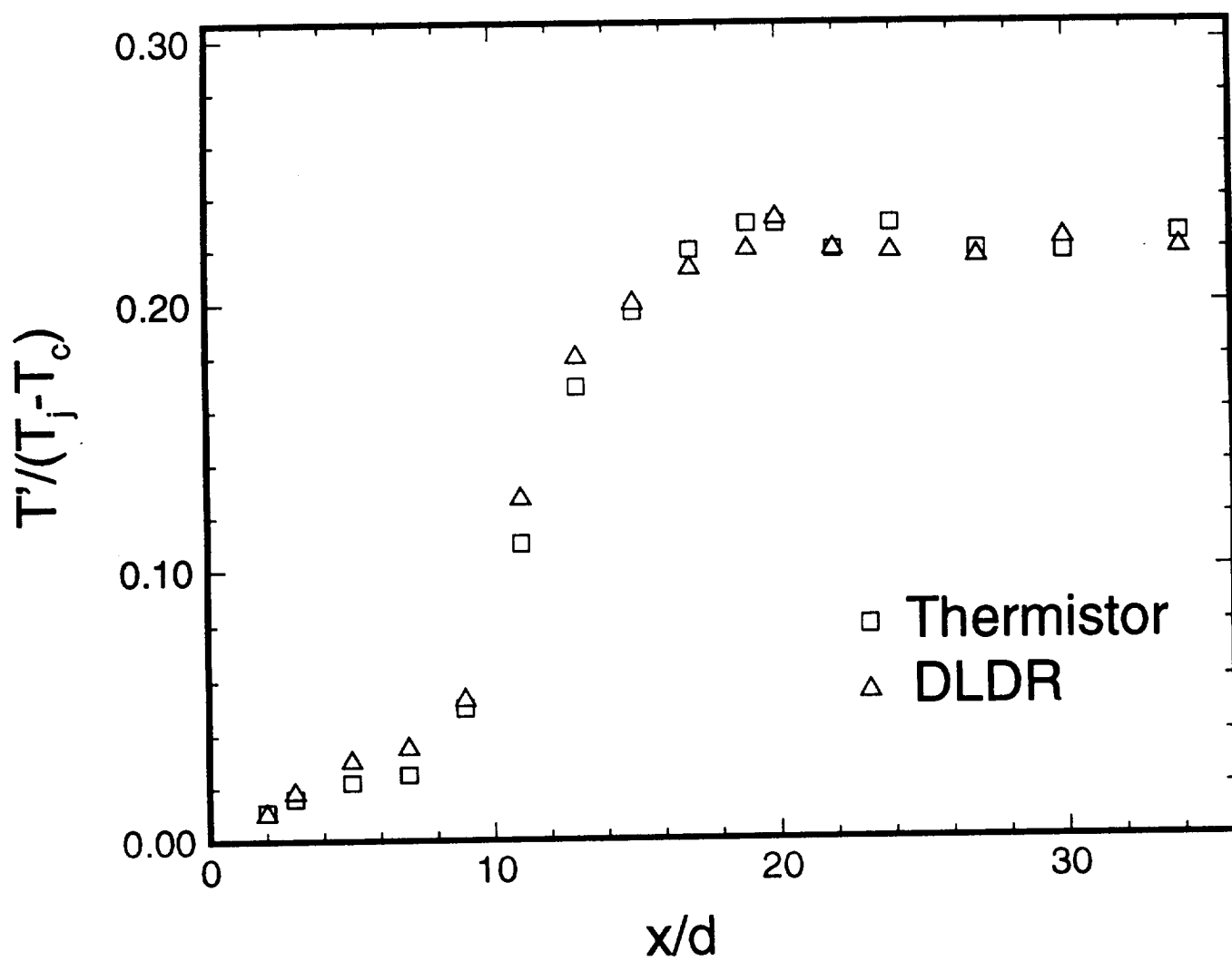
Fig. 13: RMS of jet centerline temperature

UV Filter Material Testing

Nd:YAG Laser

Seeder Laser

Mirror

9

532 / 266
532
7
532
532 / 1064
6
1064

1064

Dump

Fabry–Perot

2

Lens   Interferometer   Lens

8   532

5

Beam
Splitter

Absorption Cell

266

Beam
Splitter

3

4

Dump   Mirror

4

1

Personal
Computer

1	Digital/Analog Converter Board
2	Timing Module
3	Boxcar Averager
4	Photomultiplier Tube
5	CCD Camera
6	Second Harmonic Generator
7	Fourth Harmonic Generator
8	Harmonic Separator (532/266 nm)
9	Harmonic Separator (532/1064 nm)

Fig. 14: Experimental setup for the UV filter testing

Fig. 15: The tuning of the Nd:YAG laser observed by the Fabry-Perot interferometer
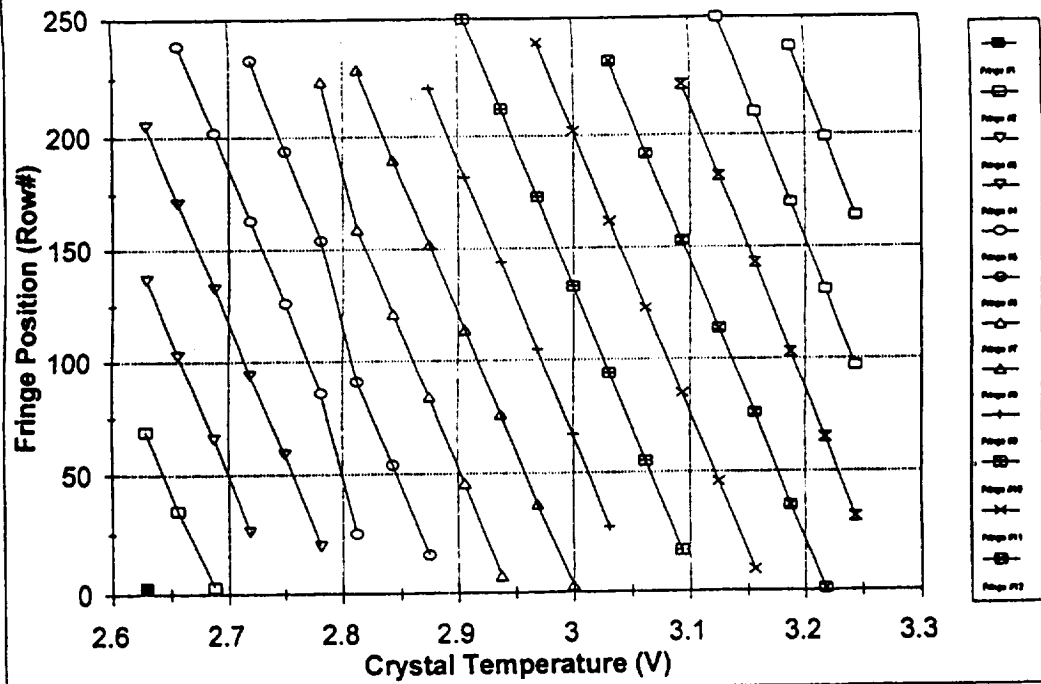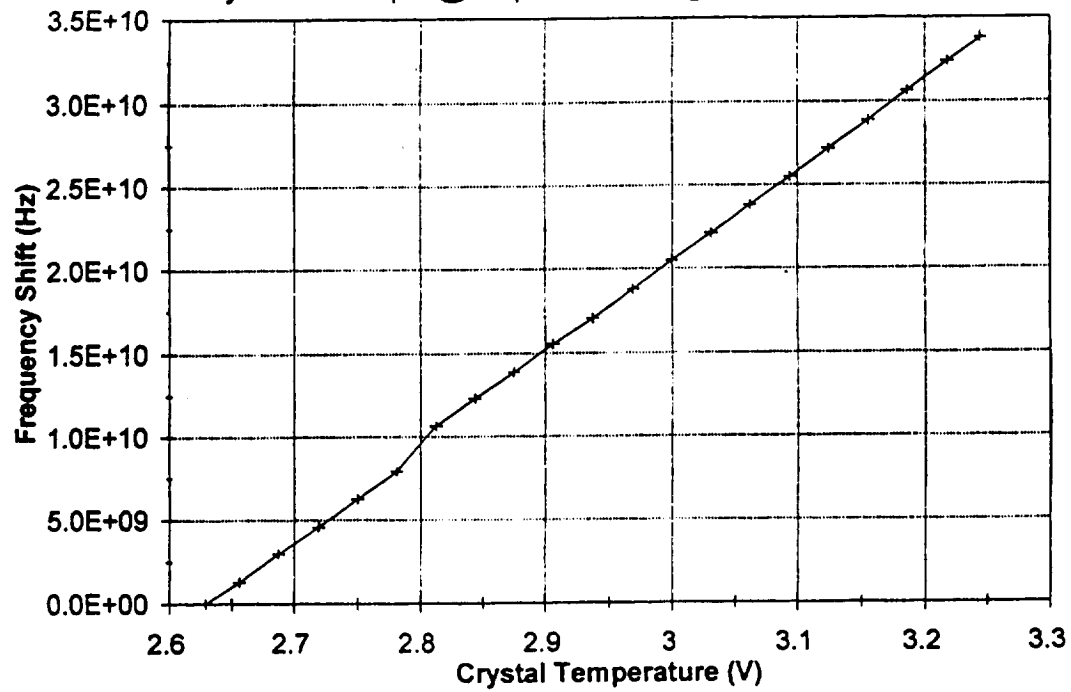
Fig. 16: Calibration plot for the laser
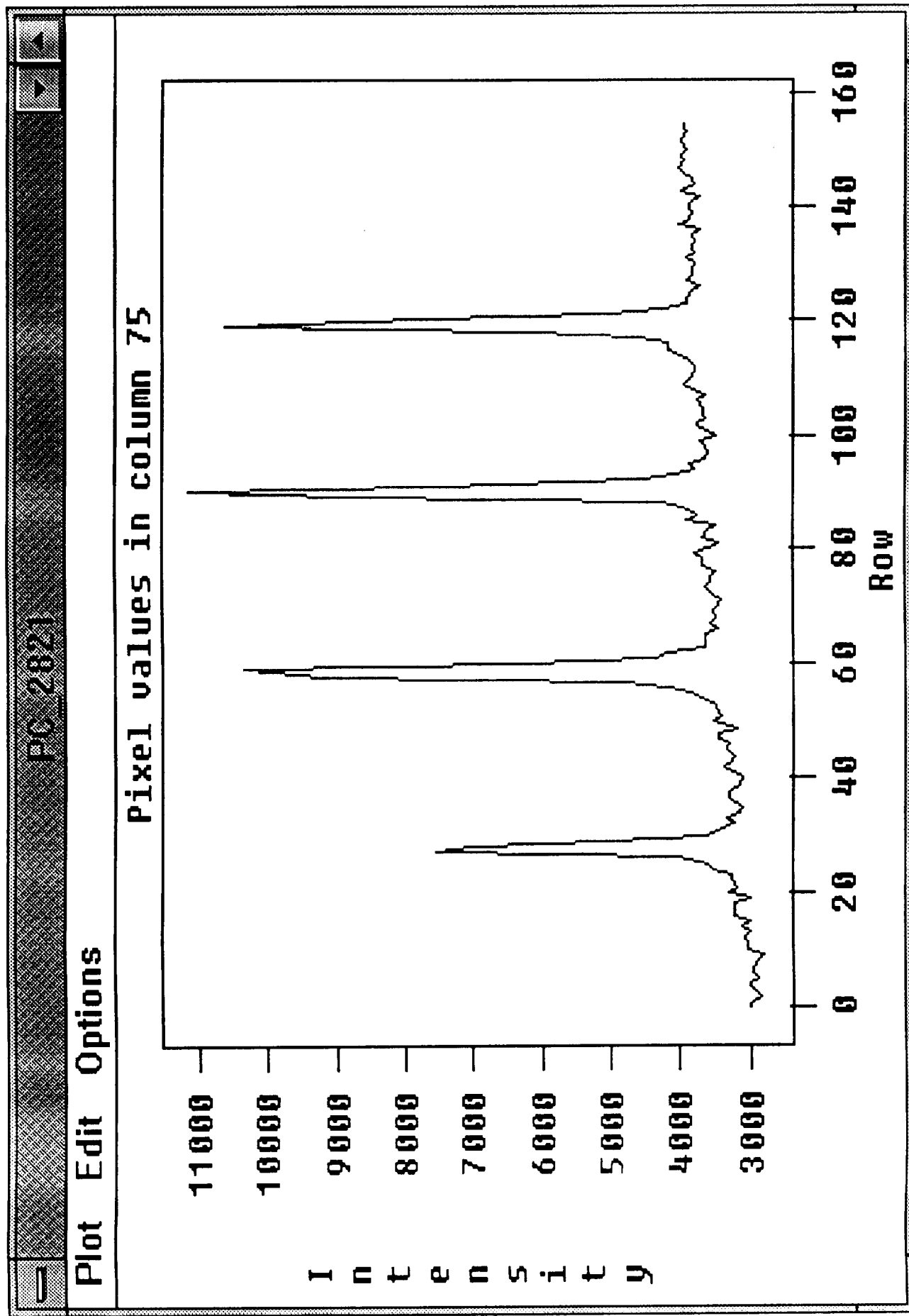
Fig. 17: Stable operation of the laser near the edge of the tuning range
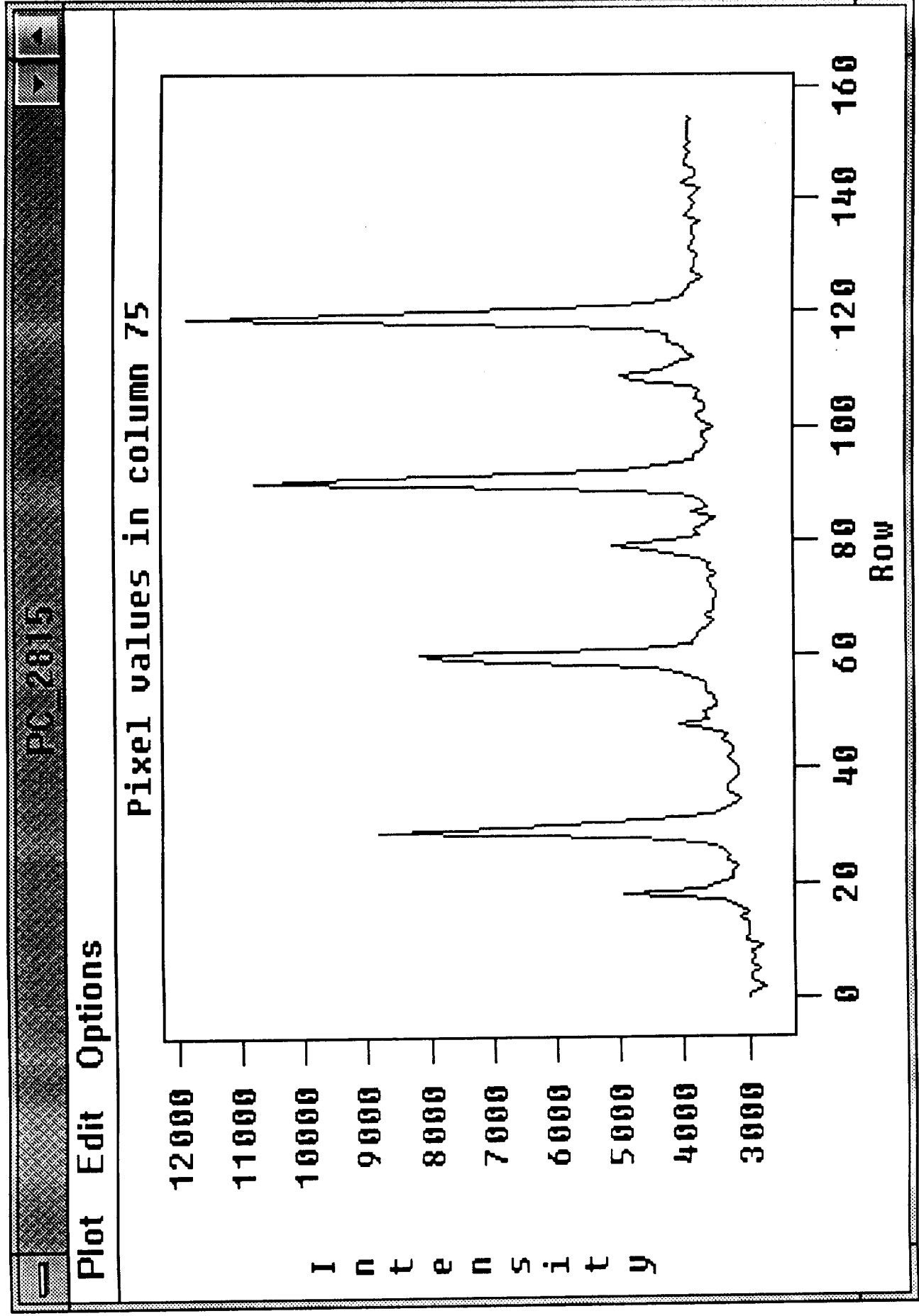
Fig. 18: Unstable output of the laser at the edge of the tuning range
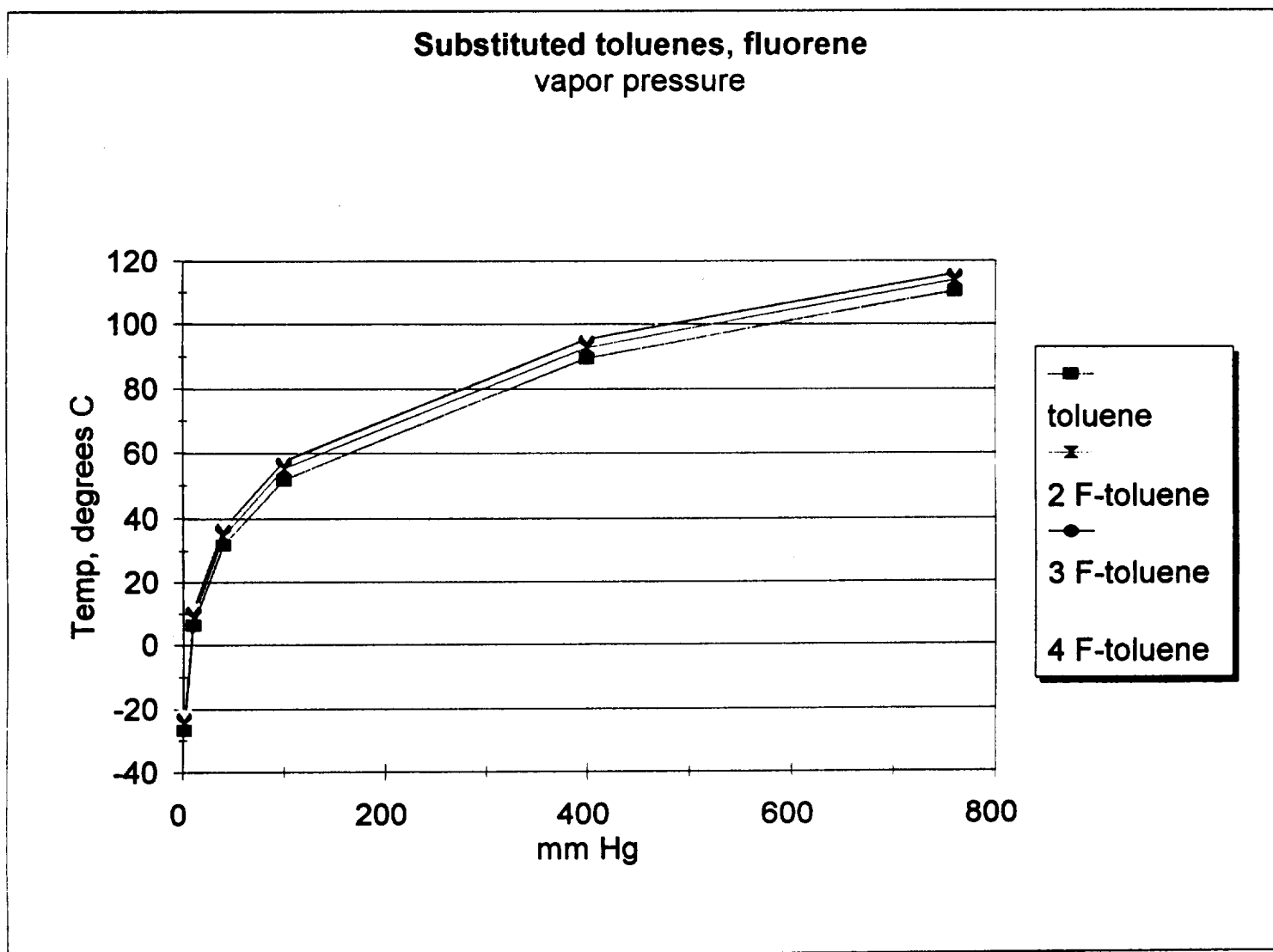
Fig. 19: Vapor pressure diagram of substituted toluenes

Fig. 20: Vapor pressure diagram for substituted benzenes
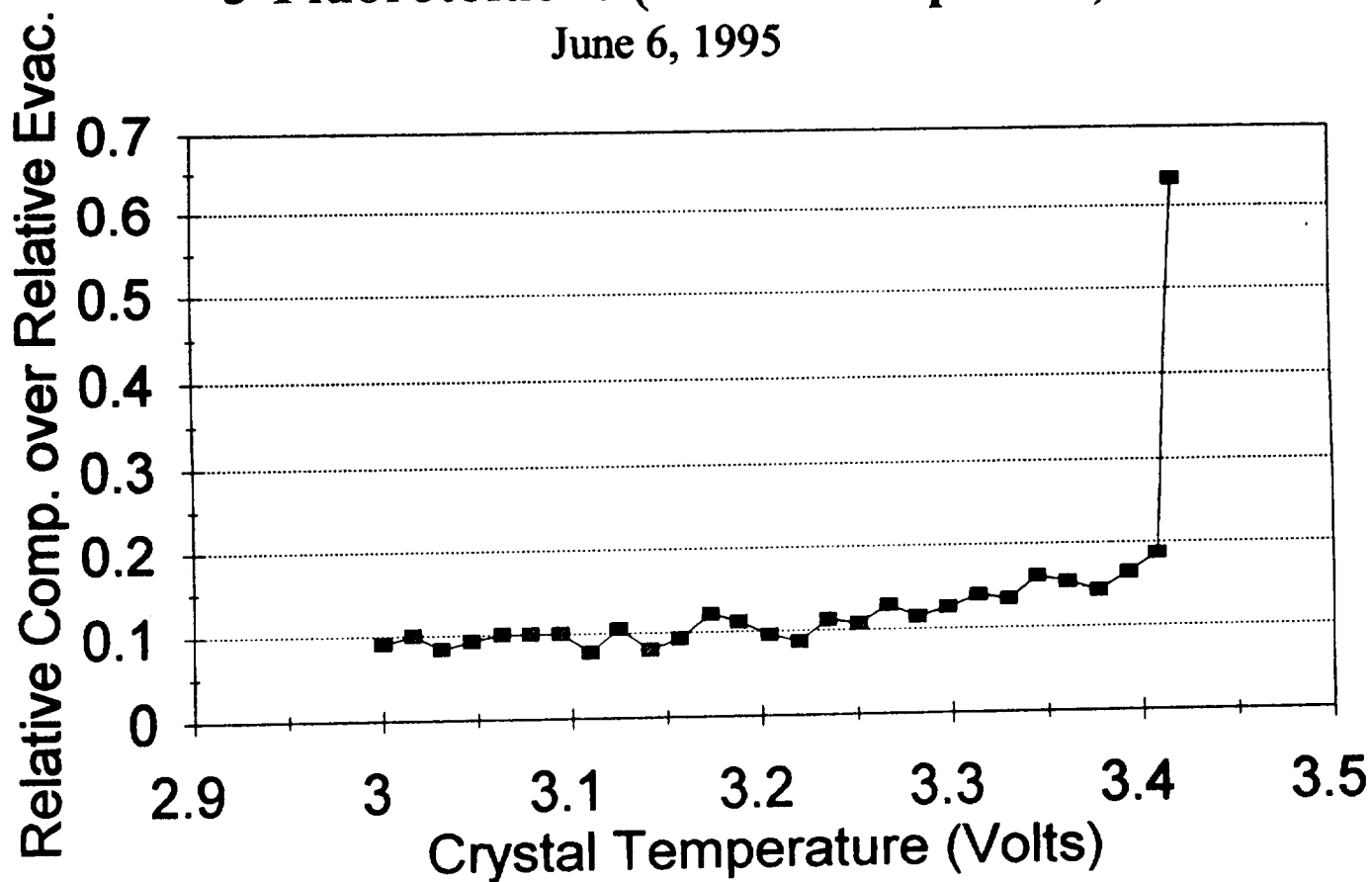
Fig. 21: Absorption characteristics of 3-Fluorotoluene at room temperature

Fig. 22: Absorption characteristics of 3-Fluorotoluene at 0 °C

Benzene (Finger at 0 C)
June 1, 1995
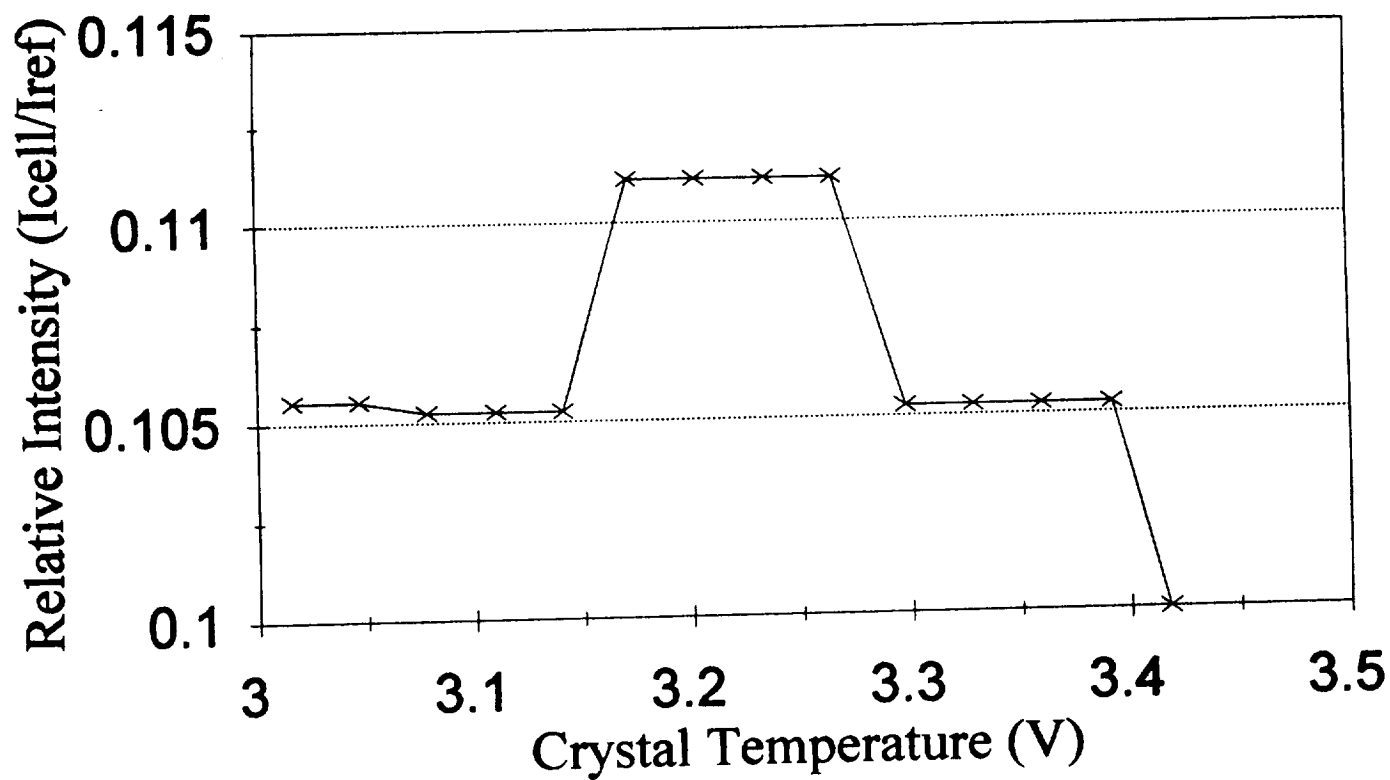
Fig. 23: Absorption characteristics of Benzene at 0 °C

Monochlorobenzene - approx 19 C

June 8, 1995
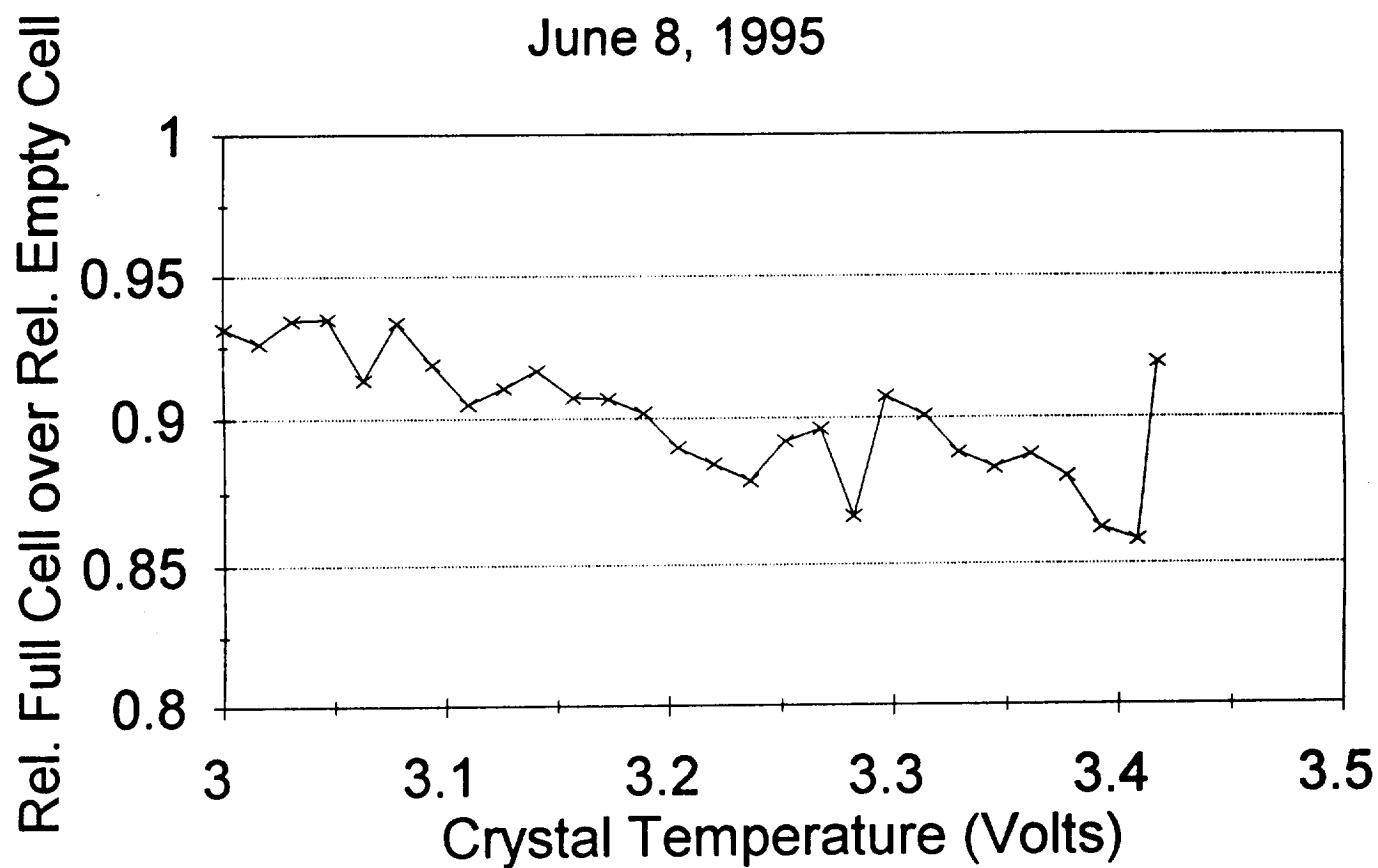
Fig. 24: Absorption characteristics of Benzene at 19 °C
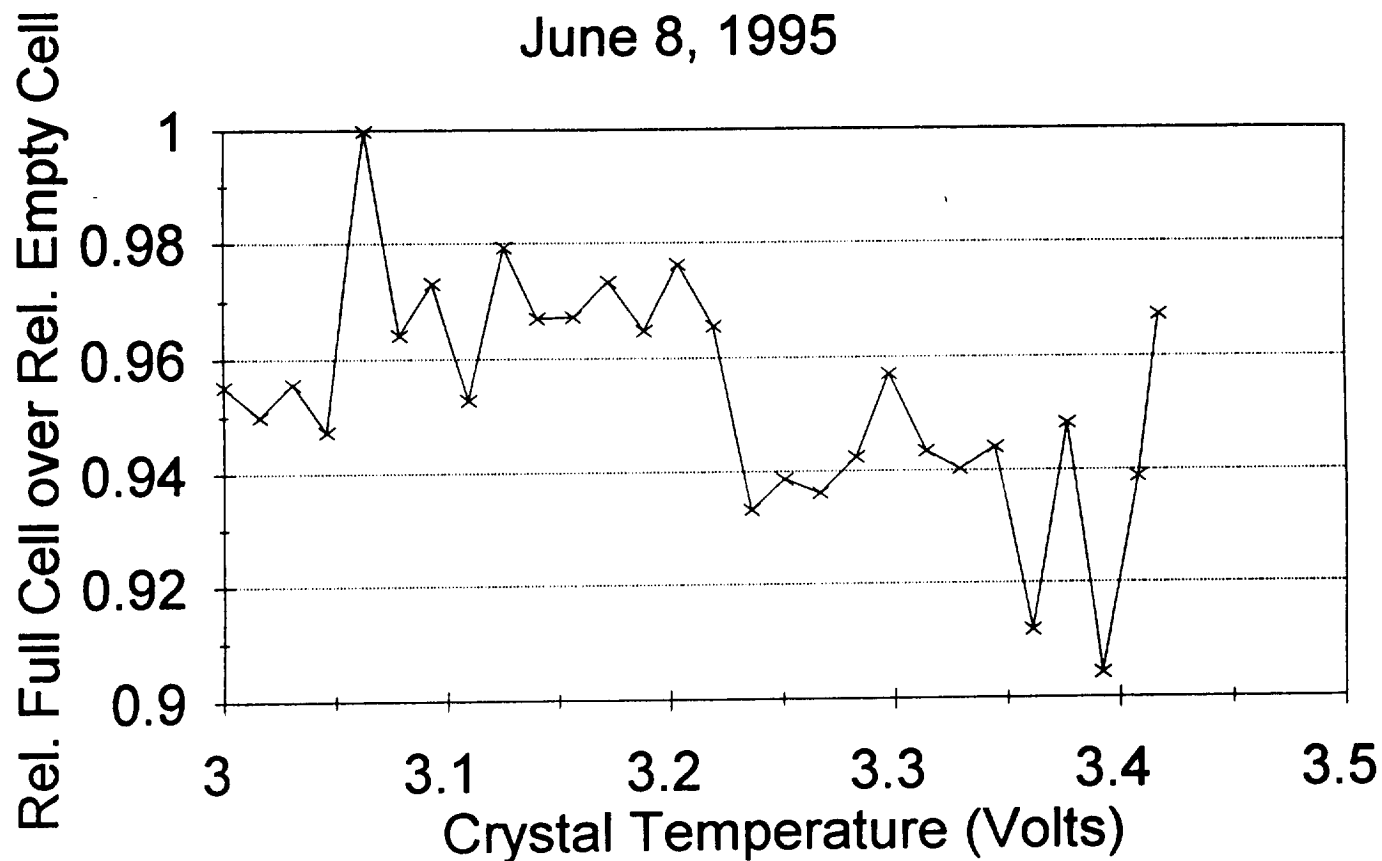
Fig. 25: Absorption characteristics of Bromo-Benzene at 19 °C
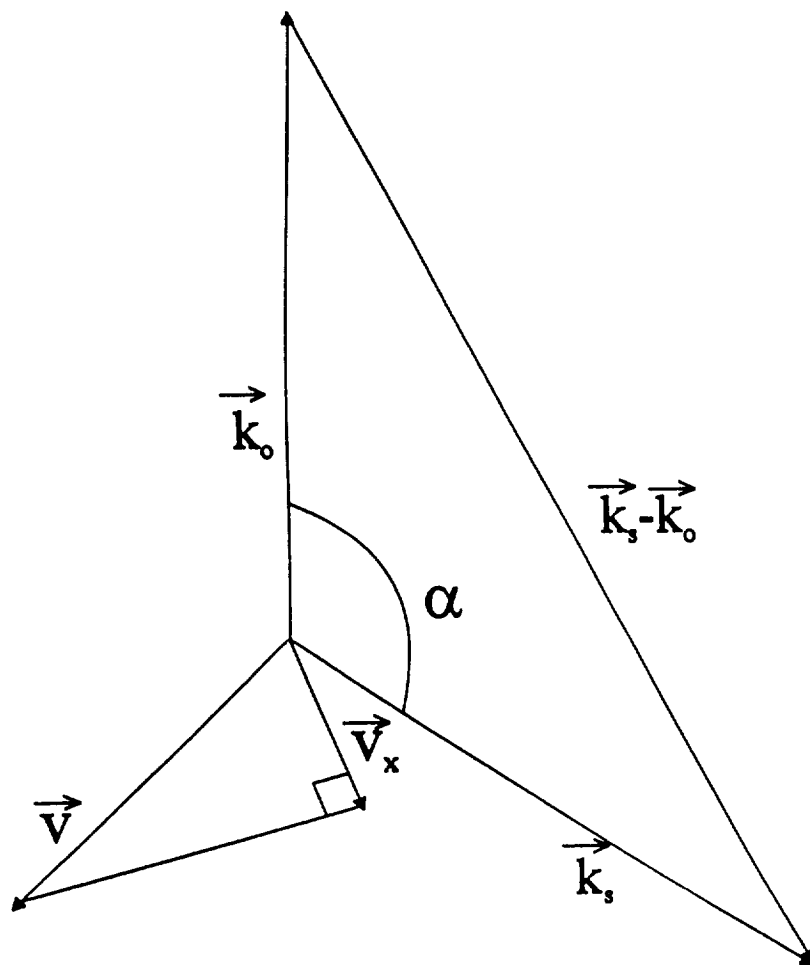
Fig. 26: Principle of Doppler shift
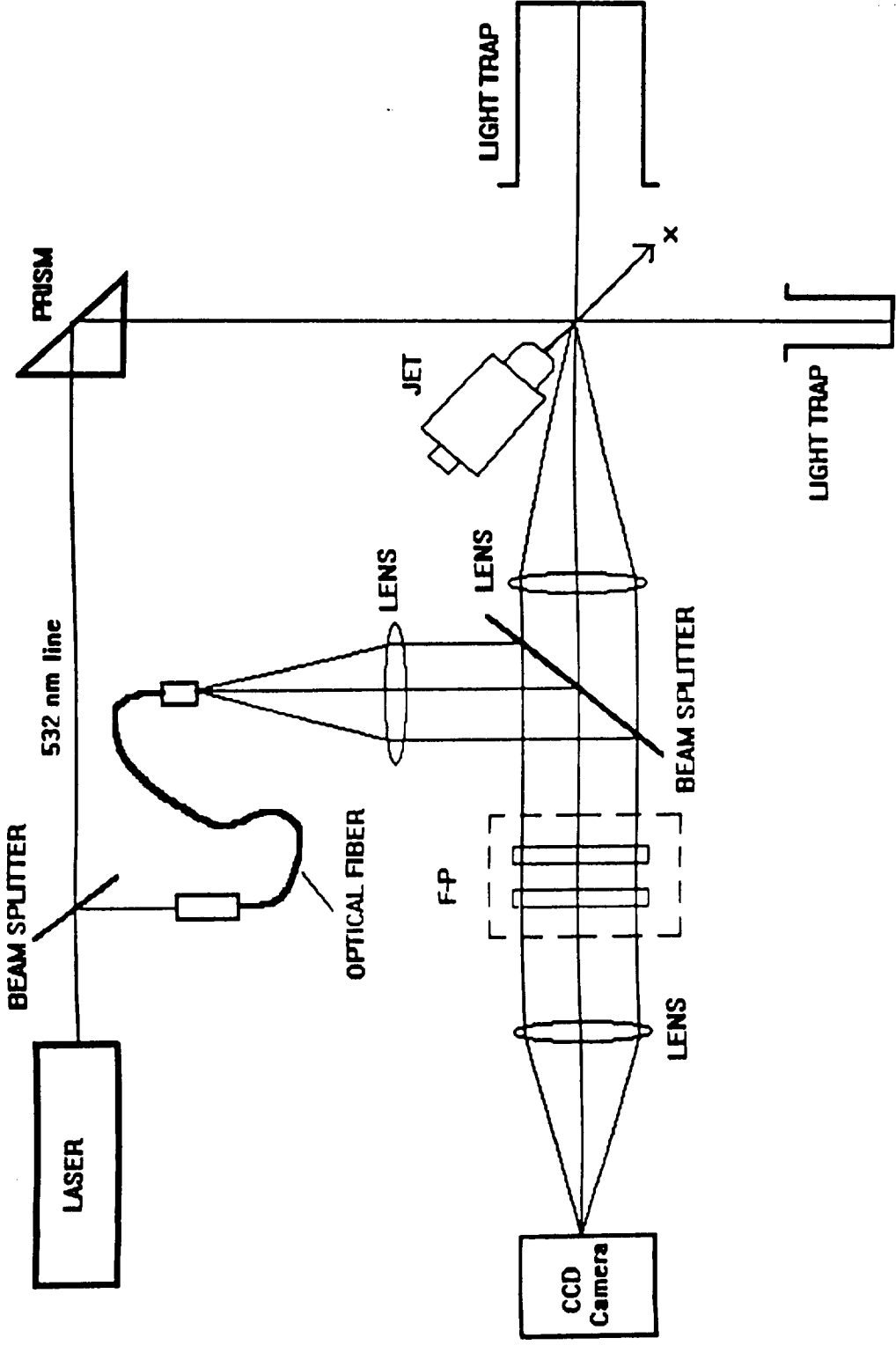
Fig. 27: Schematic of the Fabry-Perot imaging system with supersonic jet
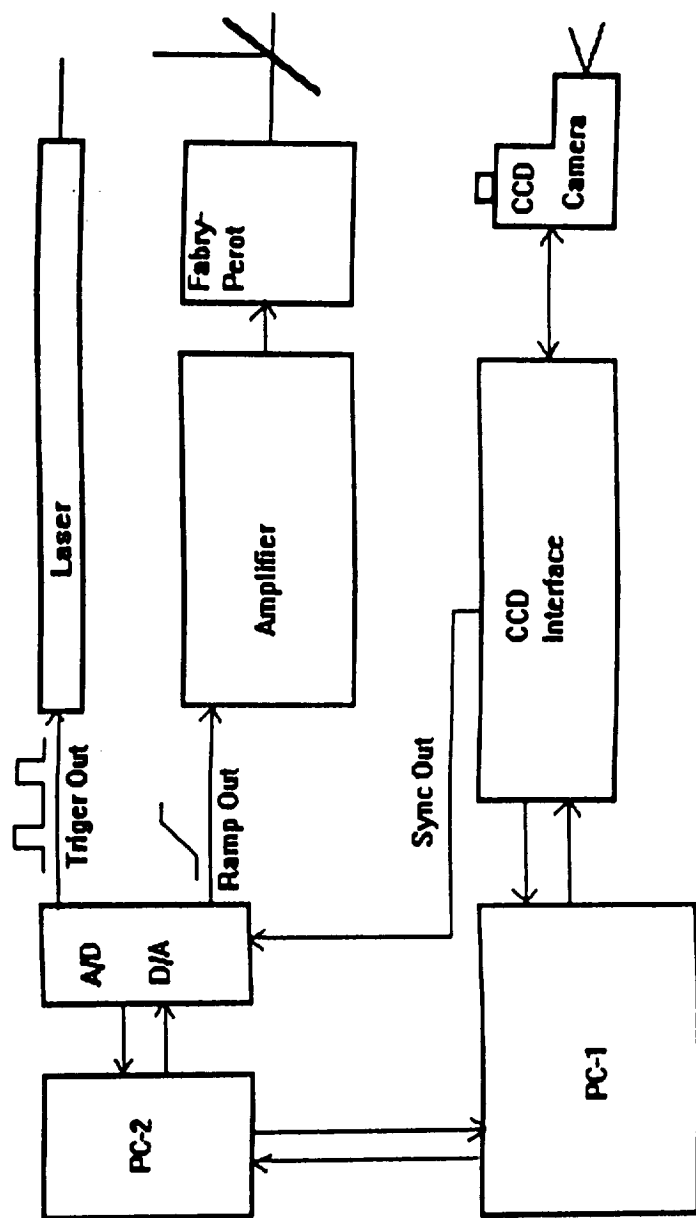
Fig. 28: Electronic arrangement for the Fabry-Perot imaging experiments
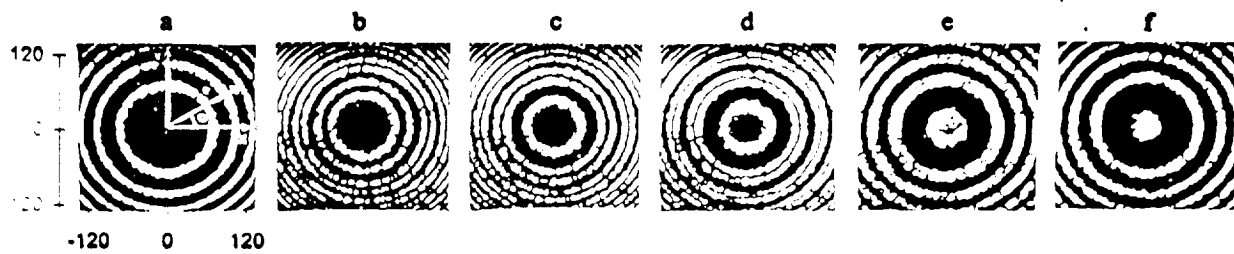
Fig. 29: Actual Fabry-Perot images
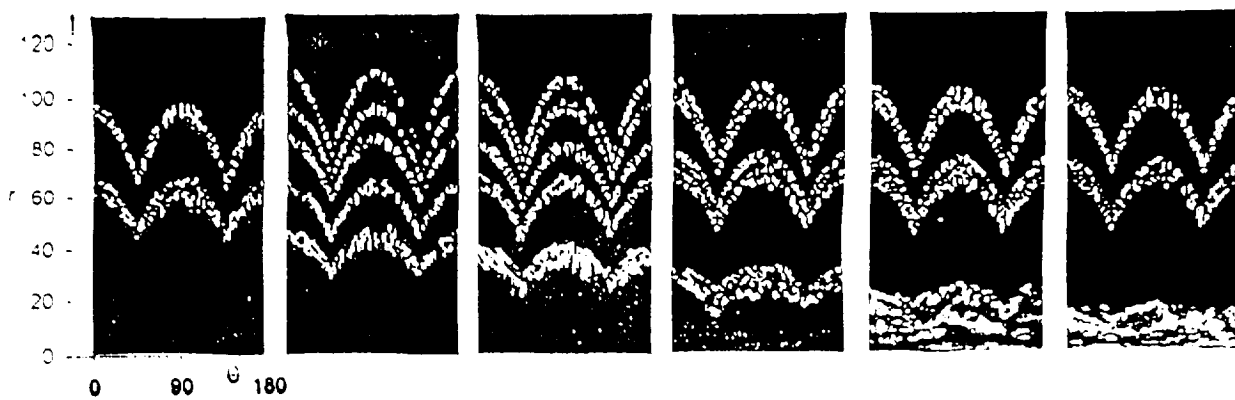
Fig. 30: Images on the r-θ plane
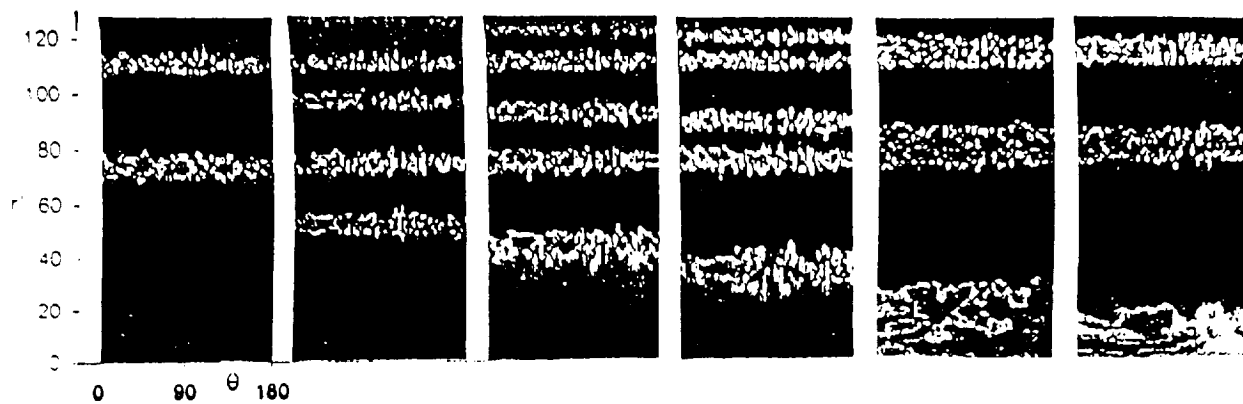
Fig. 31: r-θ images with normalized r
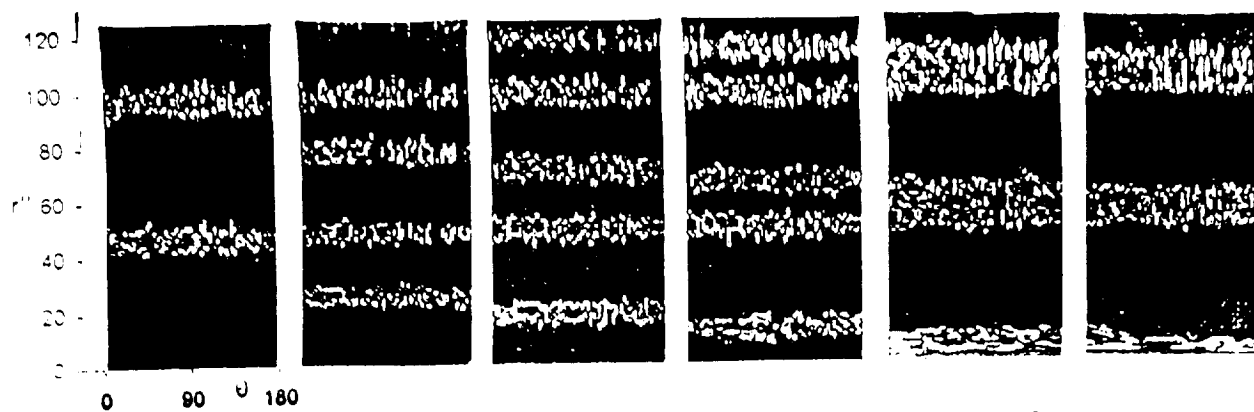
Fig. 32: Modified r-θ images according to Equation 10
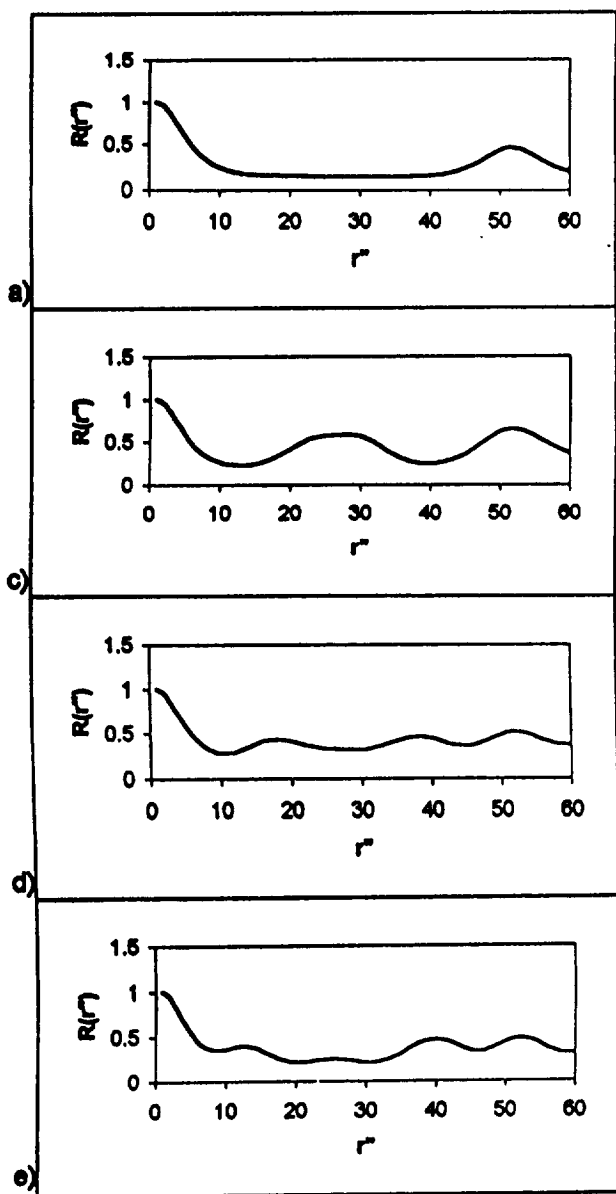
Fig. 33: Correlation functions obtained from Fig 32
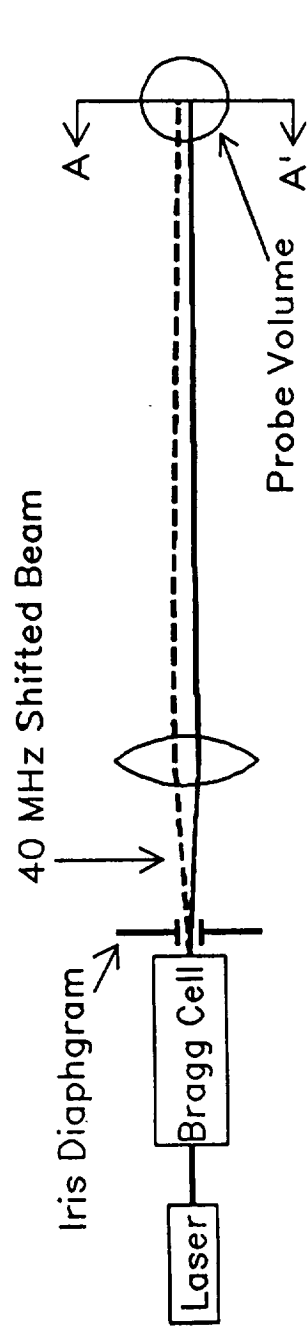
Fig. 34: Derivative of the correlation functions

x–z plane

Proportional to u

$\vec{k}_{s,1}$

α_1

$\vec{k}_{o,1}$

y–z plane

$\vec{k}_{s,2}$

α_2

$\vec{k}_{o,2}$

Proportional to v

x–z plane

y–z plane

$\vec{k}_{s,1}$

$\vec{k}_{s,2}$

$\vec{k}_{o,2}$

$\vec{k}_{o,1}$
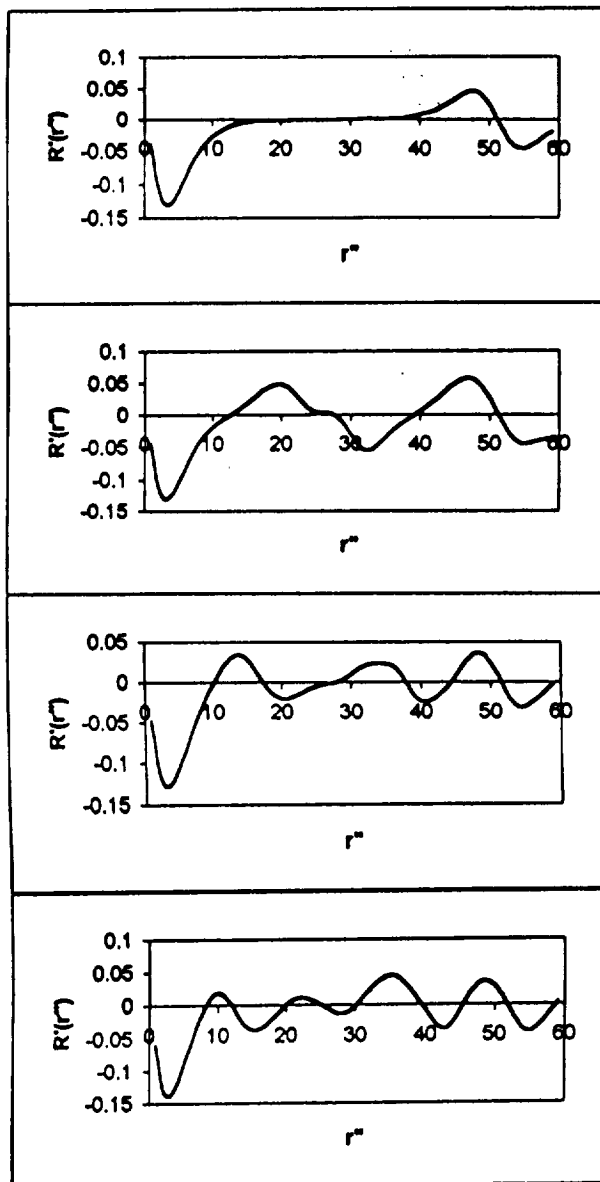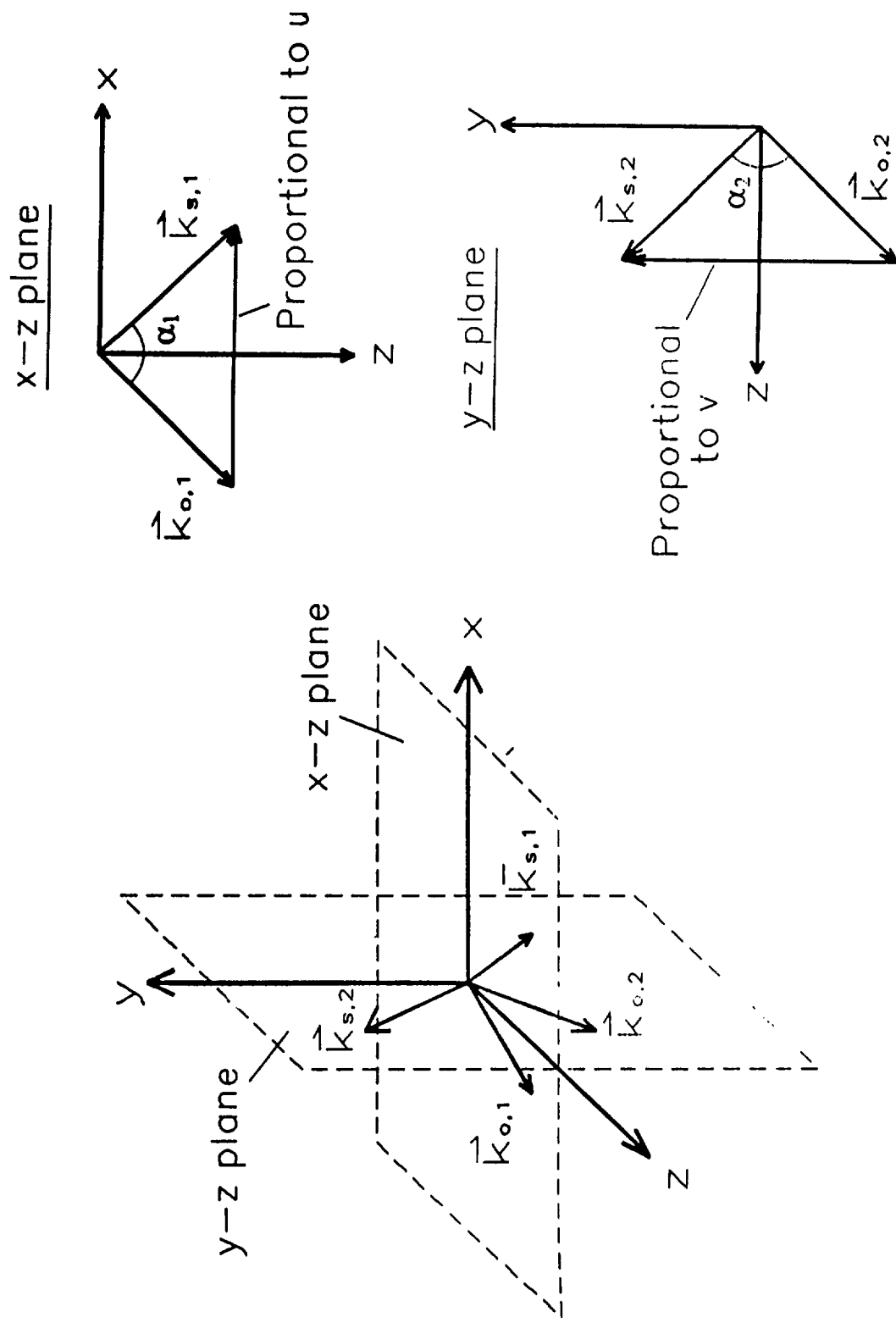
Fig. 35: Optical configuration for the vorticity probe
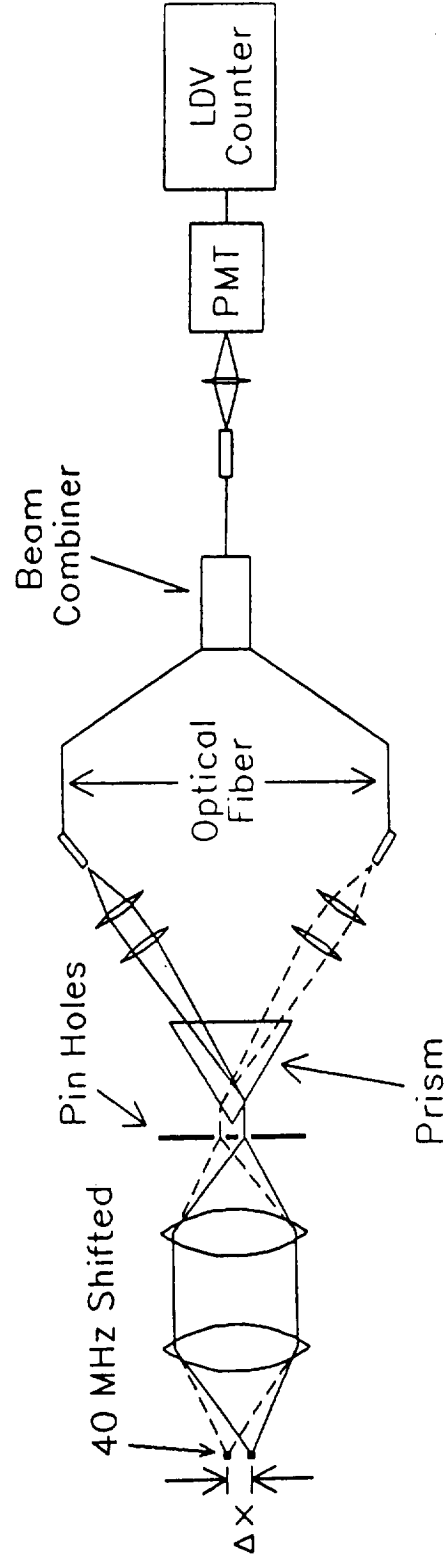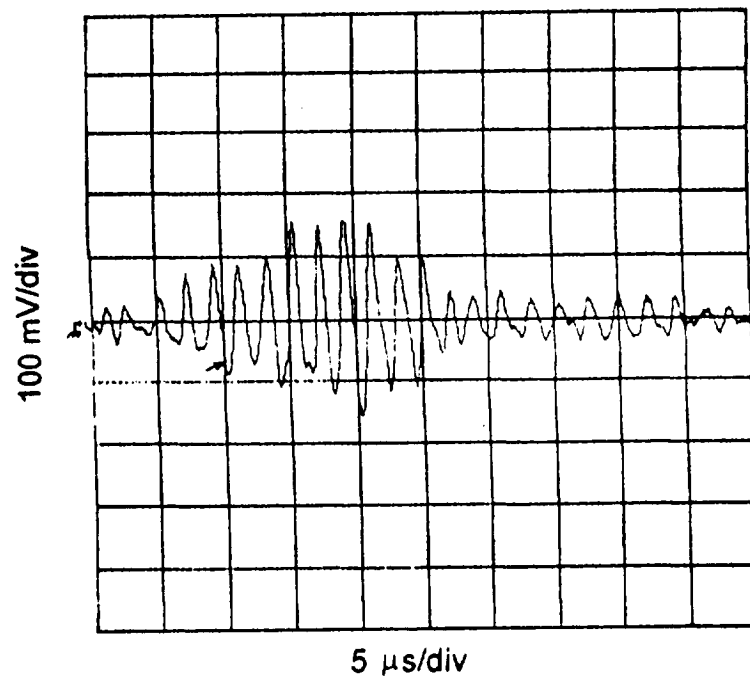
Fig. 36: Optical setup for the strain rate measurements
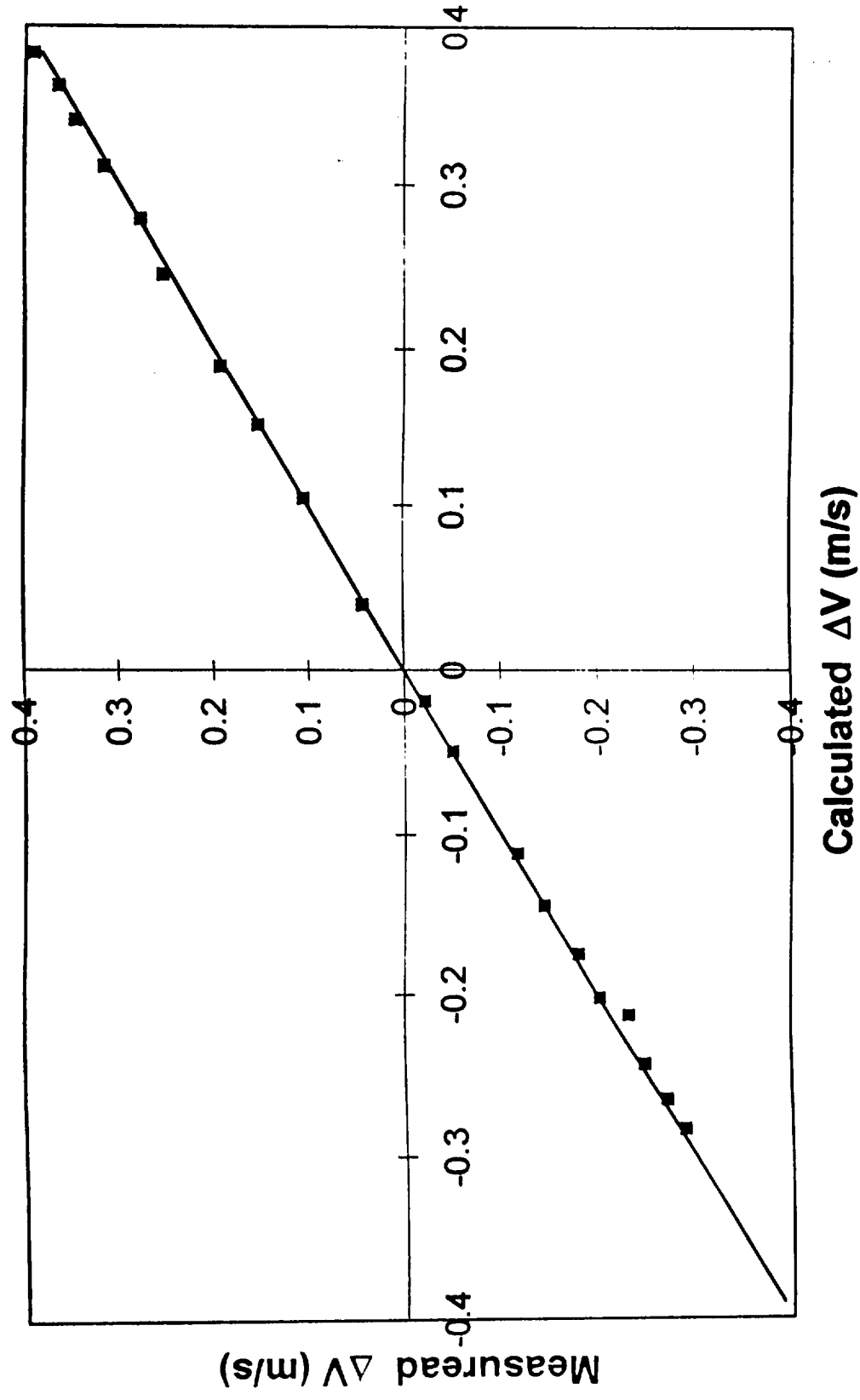
Fig. 37: Beat frequency observed on the oscilloscope

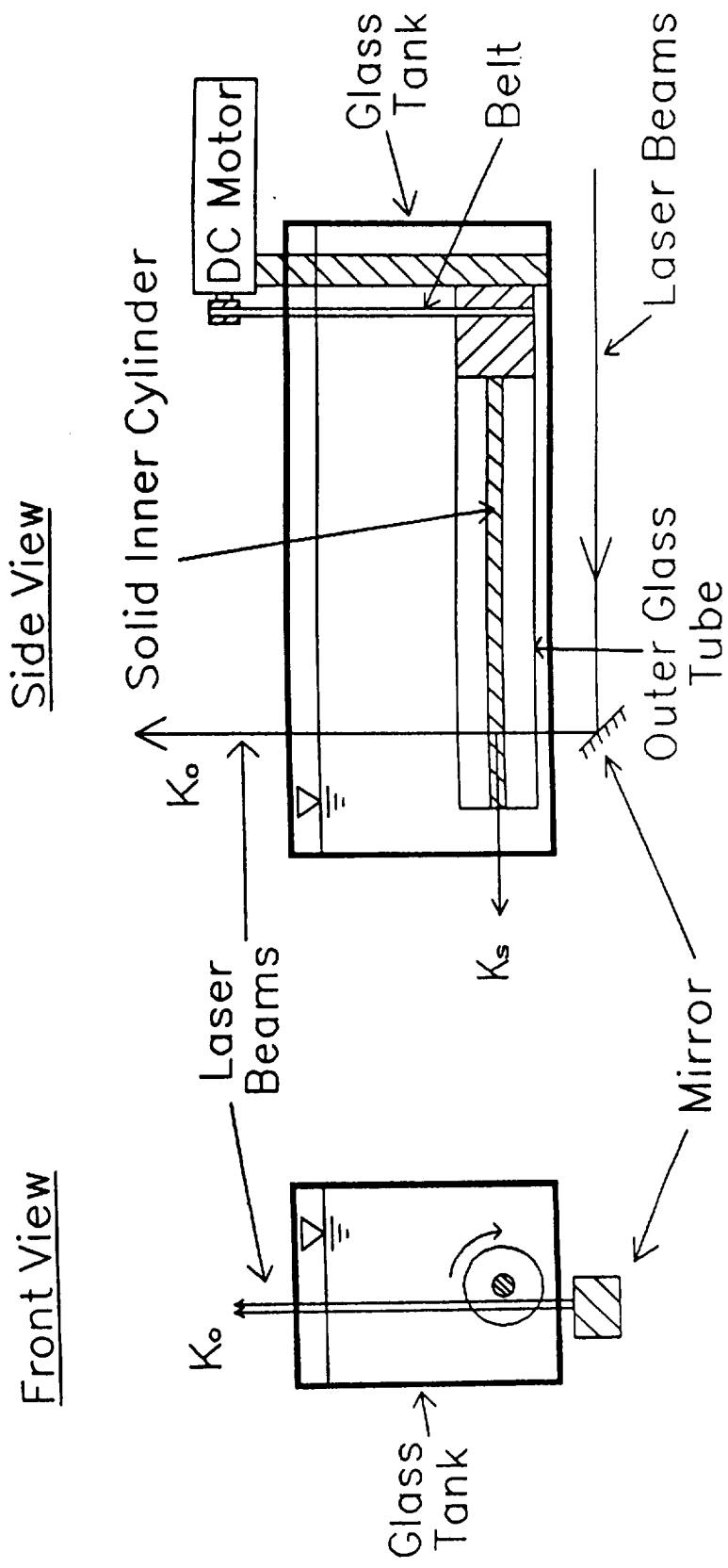Fig. 38: Comparison of measured and calculated velocity differences on rotating wire

Front View

Laser Beams

Glass Tank

K_o

Side View

Solid Inner Cylinder

DC Motor

Glass Tank

Belt

K_o

K_s

Outer Glass Tube

Laser Beams

Mirror

Laser Beams
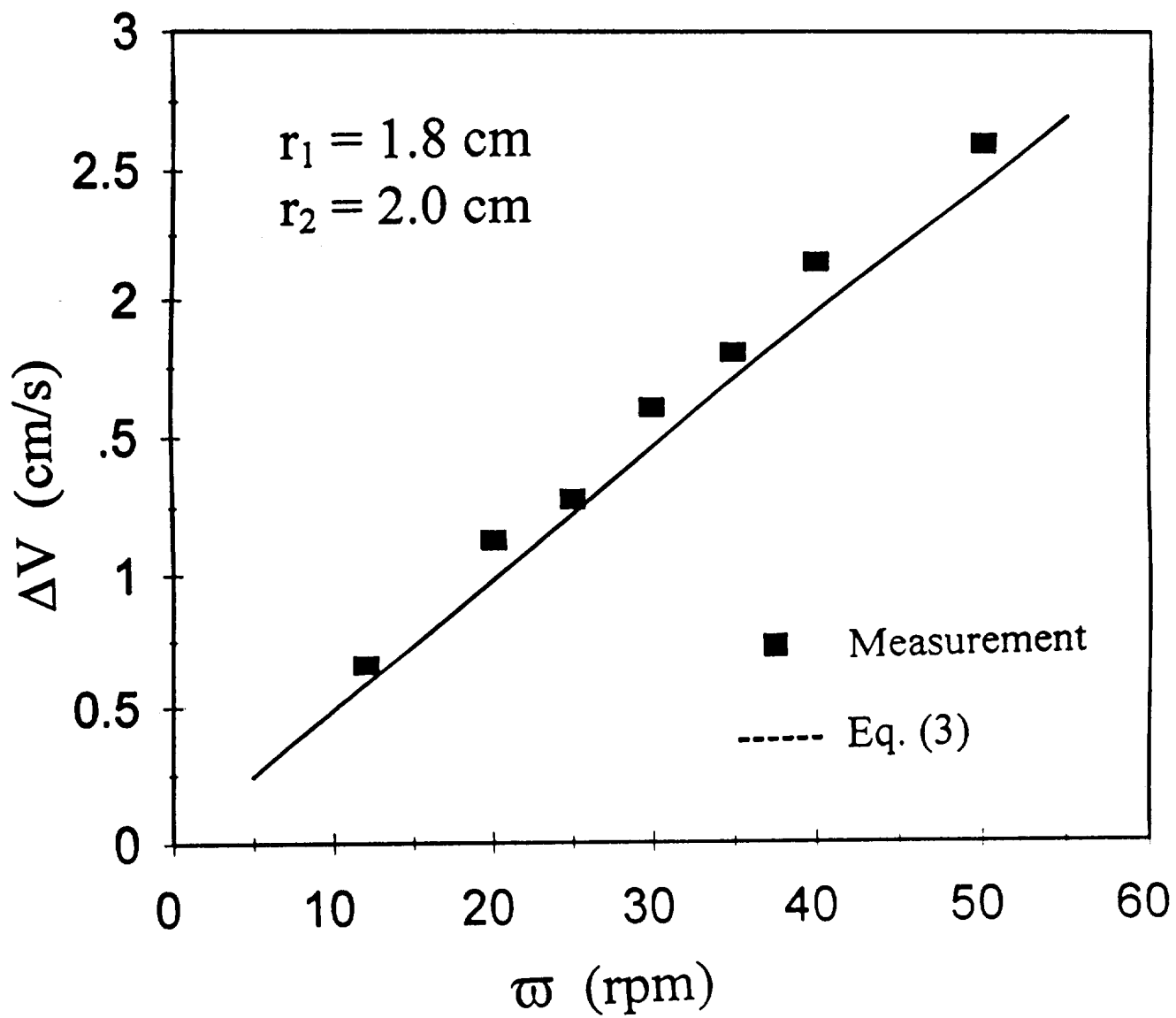
Fig. 39: Setup for the concentric cylinder experiment

Fig. 40: Comparison between measurement and the exact solution